KU LEUVEN

Buildwise

OVMONITORING.BE

MONITORING OF STRUCTURES AND ELEMENTS WITH FIBER OPTICS

– VALIDATION EXPERIMENTS –

- MONITORING OF CONCRETE STRUCTURES BY MEANS OF FIBER OPTICS -

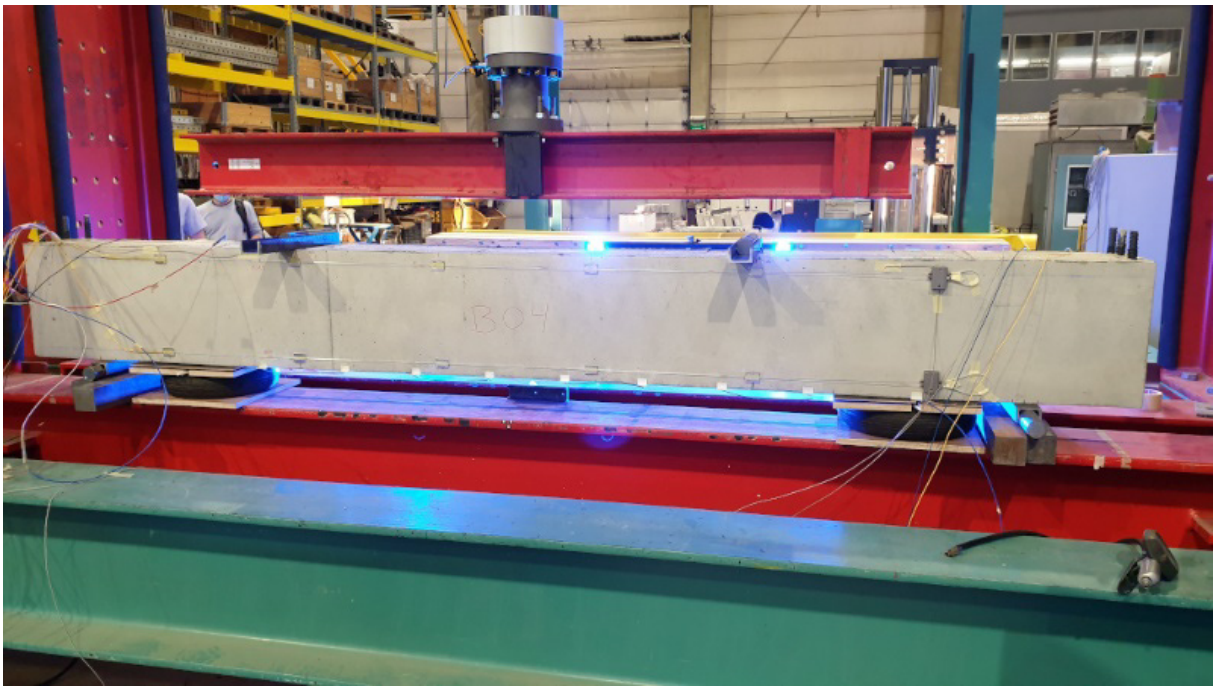

FLANDERS INNOVATION & ENTREPRENEURSHIP

Flanders State of the Art

This document has been elaborated in the framework of the COOCK project HBC.2019.2505 'Monitoring of structures and elements with fiber optics' funded by the Flemish Agency for Innovation (VLAIO).

Version 1.0

22/10/2022

Collaborators: Petra Van Itterbeeck[1], Gust Van Lysebetten[1], Noël Huybrechts[1], Dimitrios Anastasopoulos[2], Edwin Reynders[2], Stijn François[2]

[1] Buildwise, Geotechnical, Structures and Concrete Technology Division

[2] KU Leuven, Faculty of Engineering Science, Structural Mechanics Subdivision

Version 1.0

Date: 22/10/2022

Contact: petra.van.itterbeeck@buildwise.be or gust.van.lysebetten@buildwise.be

Table of Contents

1 Introduction

In order to evaluate the performance of optical fibres for the monitoring of concrete structures, several validation tests were performed at different levels. Different optical fibre setups and types were evaluated in a real reinforced concrete environment. In addition, special attention was also dedicated to concrete-specific damage phenomena, in particular, the ability of optical fibres to detect crack formation and corrosion.

1.1 Concrete beam and fibre optics setup

Four reinforced concrete beams were equipped with a wide range of fibre optics. The reinforcement detailing of the beams as well as the mechanical characteristics and composition details of the concrete can be found in Figure 1.

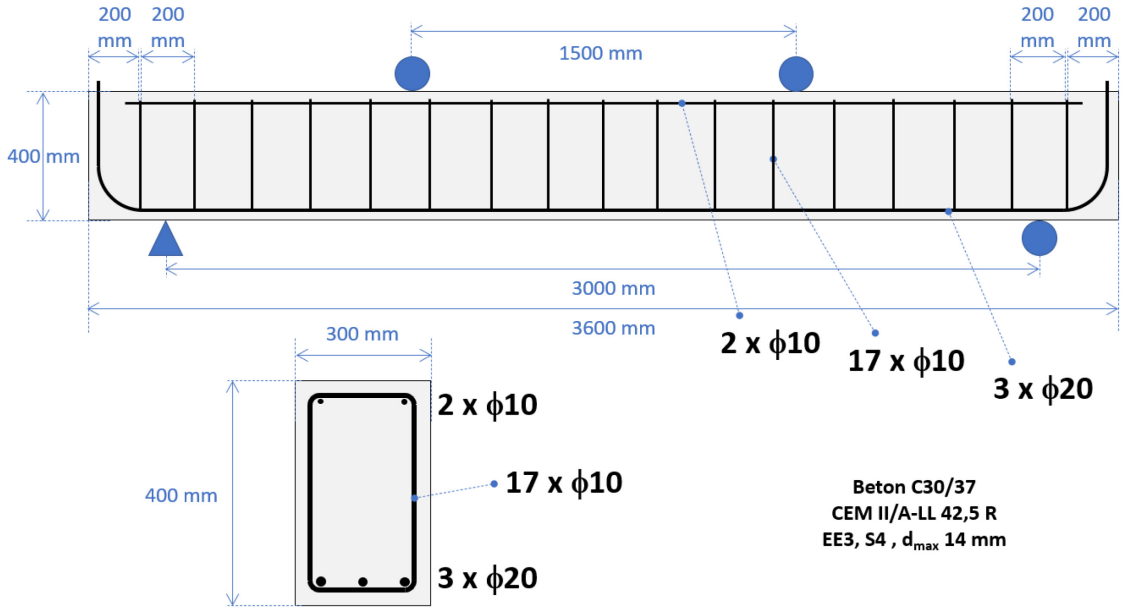

Figure 1. Reinforcement detailing of the concrete beams

The optical fibres were both installed on the reinforcements in the concrete as well as mounted on the concrete surface. A schematic overview of the embedded optical fibres and their setup can be found in Figure 2. In the 4 corners of the section, 2 types of BOFDA optical fibres were installed, of the type Flat and V9. More technical details of these two fibre types can also be found in Figure 2.

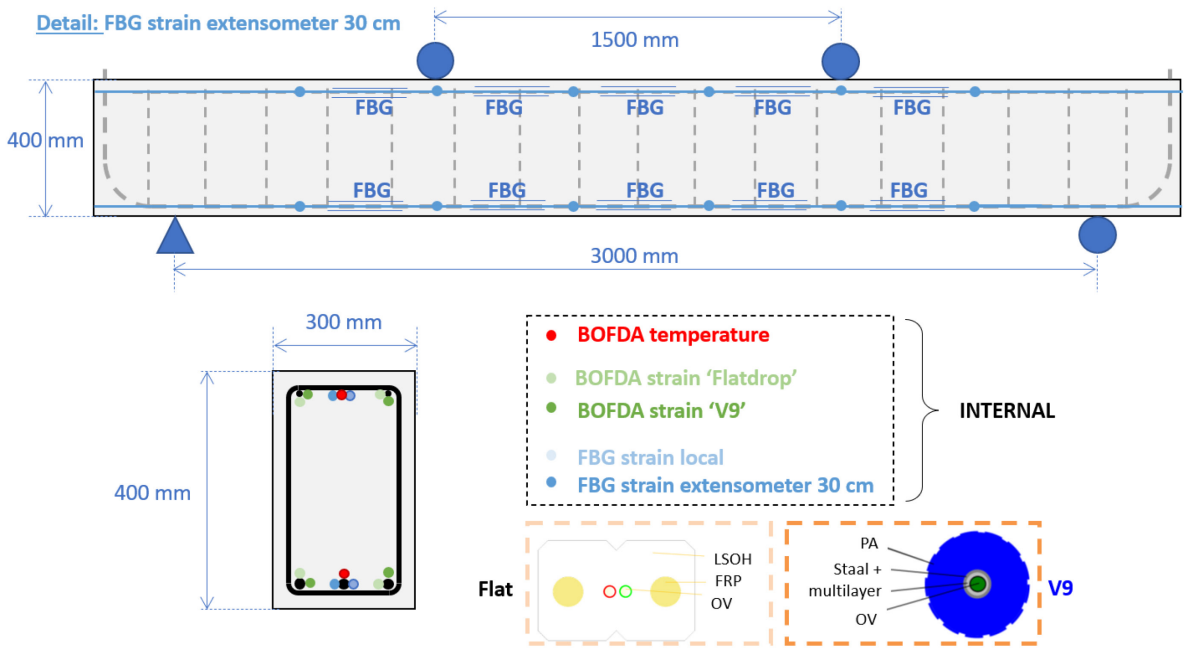

Figure 2. Schematic representation of the built-in optical fibre measurement lines.

Central, at the top and bottom in the section of the concrete beam, two FBG measuring lines were installed as well as a BOFDA temperature cable. For these FBG measuring lines, the optical fibres were glued into a support rod, in order to achieve a more robust arrangement that could withstand concreting activities (see Figure 3). For one of these two FBG measuring lines, tubes of +/- 30 cm were also fitted around the carrier rod this specifically at the locations of the FBG inscriptions (which are spaced 50 cm apart on the optical fibre). This construction was selected for testing in order to evaluate whether the carrier rod could be locally decoupled from the concrete in this way to achieve a semi-extensometer setup. To further reduce friction between the carrier rod and the tube, a Teflon spray was locally sprayed onto the carrier rod before positioning of the tube. Heat shrink tubes were also placed over both ends of the tubes to prevent mortar seepage between tube and carrier rod (see Figure 3).

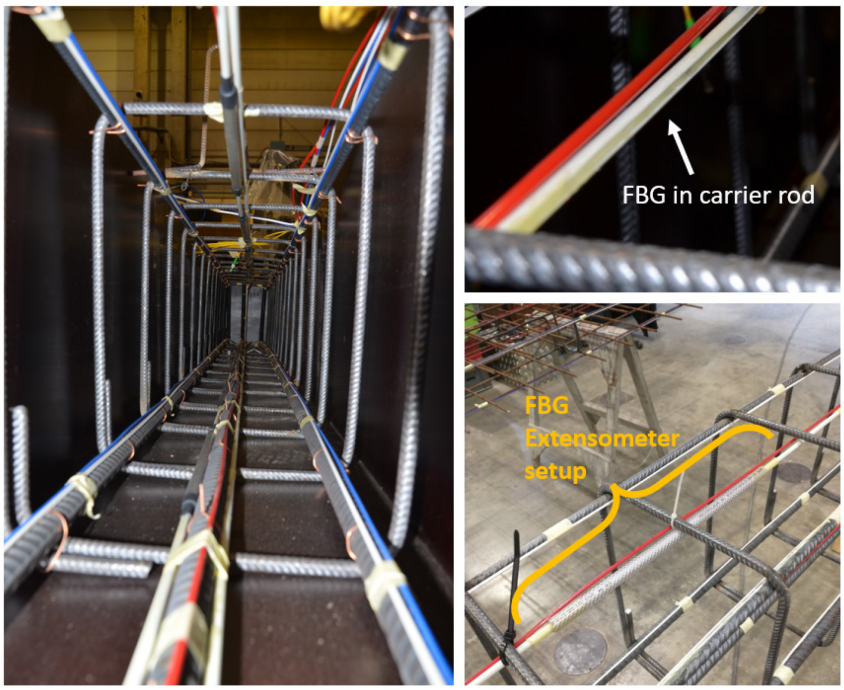

Figure 3. Photographs of the embedded optical fibre measurement lines, with a detail of the FBG in carrier rod at the top right and a detail of the FBG extensometer setup at the bottom right.

Four FBG measuring lines were also attached to the concrete surface, at the top and the bottom of the surface (at the level of the longitudinal reinforcements), and this at the front and at the rear of the beam. These FBG measuring lines are glued to the concrete surface by means of mounting blocks (see Figure 4(right)). Prestressing devices are positioned at both ends of the beam in order to provide a certain degree of pre-stressing to the measuring lines (see Figure 4(left)). The mounting blocks are located centrally between the FBG inscriptions. At the front and rear of the beam, the FBG inscriptions are respectively positioned at an interval of 25 and 50 cm.

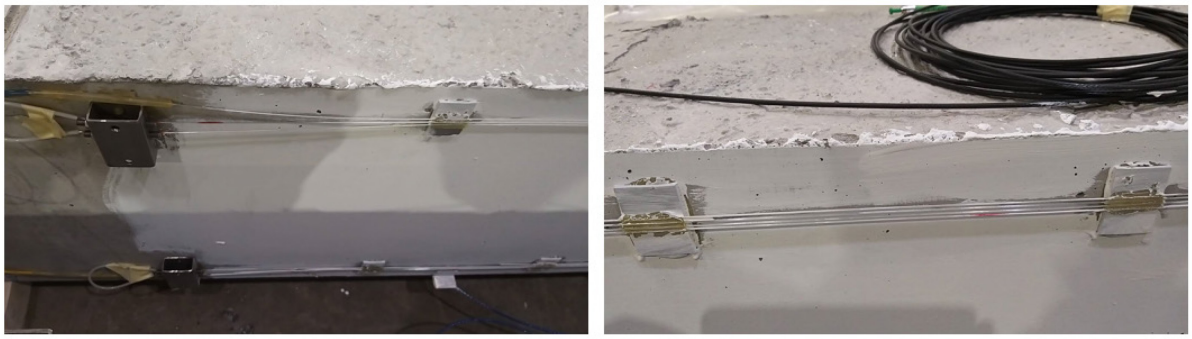

Figure 4. Photographs of the optical fibre measurement lines mounted on the concrete surface, (left) prestressing device at the end of the beam, (right) extensometer attachment using glued mounting blocks.

1.2 Reference test (static and dynamic)

One of the 4 reinforced concrete beams was subjected to a 4-point bending test in which the beam was gradually loaded to higher load levels (with a loading interval of 50 kN), this to progressively introduce damage in the beam. Upon reaching each load level, the load was held (in displacement control) and this for a few minutes in order to collect some stable (static) BOFDA measurements. The beam was then fully unloaded after each loading step to perform a dynamic measurement after which the beam was loaded again to the next load level. A preliminary analytical calculation of the cracking moment was performed. This indicated that cracks would be initiated at a loading of +/- 70 kN. The first load level was therefore chosen below this loading i.e. at a load of 50 kN. In Figure 5 the force and deflection curve can be found as a function of time.

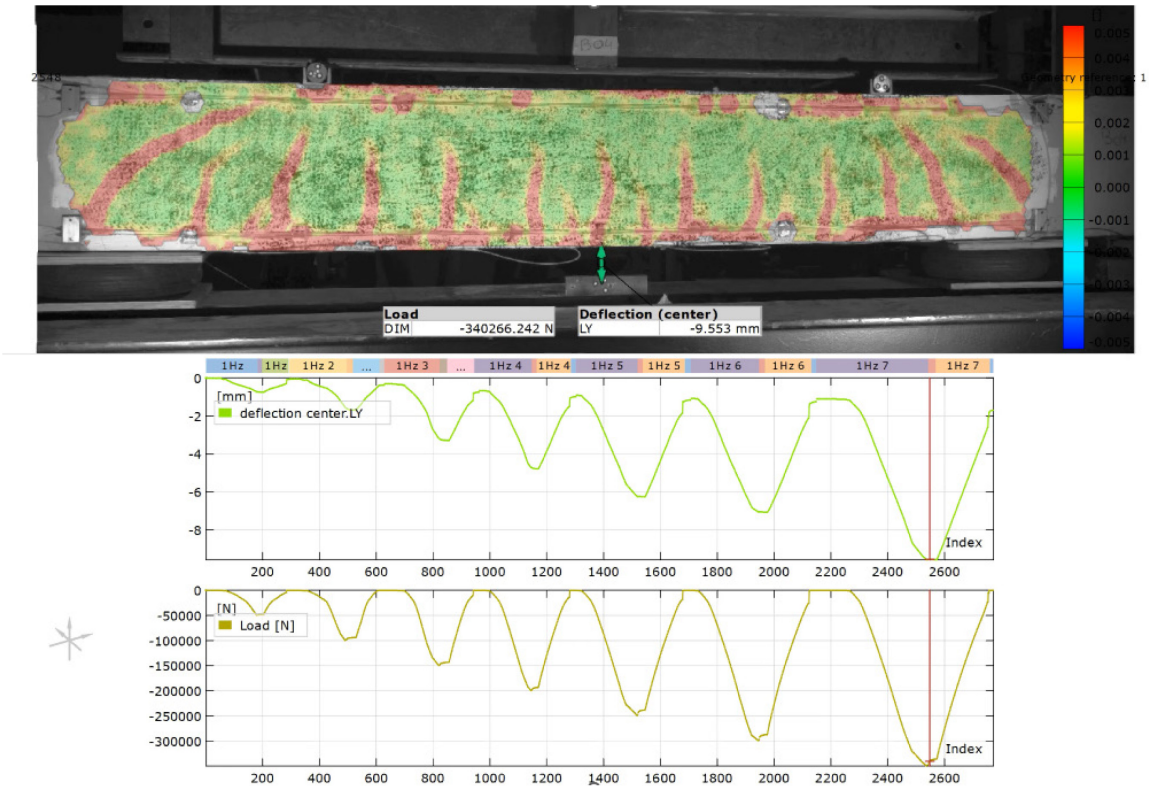

Figure 5. (Below) Load and deflection registered during the experiment in function of time. (Above) The strain profile obtained with the DIC during the last load step (at 350 kN).

The static optical fibre measurements were compared with Digital Image Correlation (DIC) measurements conducted on one of the surfaces of the beam. The concrete surface between the 2 point loads was for this purpose coated with a black and white speckle pattern. Two high-definition cameras took pictures of the speckle pattern at a selected time interval. Movements and deformations of the unique pattern of black speckles are monitored between the photos and post-processed with the supplied software package into full-field 3D strains. The strain profile obtained with the DIC during the last load step (at 350 kN) can also be found in Figure 5(above). The red areas indicate the locations of the various bending cracks.

Before starting the progressive damage test and after each unloading phase, as mentioned earlier, the beam was subjected to dynamic tests so as to identify its modal characteristics, i.e., natural frequencies and strain mode shapes, which represent the state of the beam after each loading step. For the dynamic tests, the beam was placed on flexible supports, i.e., two inflated tires (see Figure 6). They act as vibration isolators, such that uncertainty in the boundary conditions due to interaction with the supporting laboratory structure is avoided as much as possible. The dynamic free-free boundary conditions that are introduced in this way after each loading cycle, ensure that all changes in modal characteristics will only be damage-related. The dynamic excitation of the beam was performed with the use of impulse hammer impacts. The developed dynamic strains were measured only with the external FBG chains that were attached to two sides of the beam.

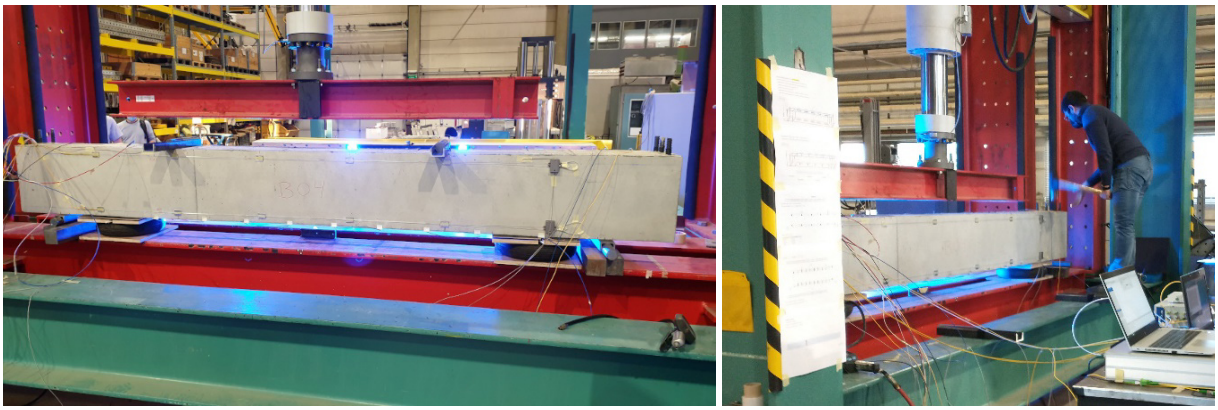

Figure 6. The experimental setup for the dynamic testing.

1.3 Corrosion experiments (static and dynamic)

Three beams were subjected to accelerated corrosion caused by an electrical corrosion process. For this purpose, the beams were placed with their undersides in a salt water bath (5% NaCl). At the bottom of this bath, a stainless steel plate was placed which is connected to the negative pole of a DC power source. The positive pole of this power source is in turn connected to the longitudinal reinforcement bars of the beam. The reinforcement will act as a result as an anode, while the stainless steel plate will become a cathode. The electrolyte (salt water) will transport OH- ions to the Fe++ charged rebars, which will lead to the development of corrosion products. The beam rests on two PVC rollers which are placed on the stainless steel plate, thus avoiding direct electrical contact with the beam. Some photos of the accelerated corrosion setup can be found in Figure 7.

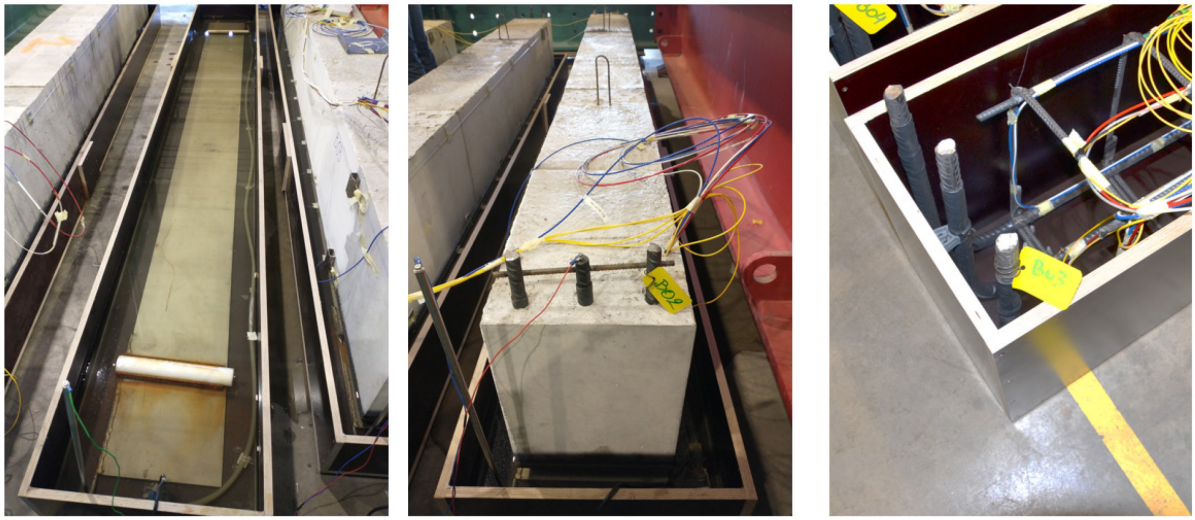

Figure 7. Accelerated corrosion setup (left and middle) blue/green cable connects the stainless steel plate to the negative pole of a DC power source and red cable connects the longitudinal rebars to the positive pole of the DC power source, (left) visual of pvc rolls and stainless steel plate, (right) heat shrink tubes provided at the anchorage of the longitudinal rebars to prevent corrosion in this part of the rebar.

A constant current was imposed between the reinforcements and the stainless steel plate. This current was gradually increased during the accelerated corrosion test. The evolution of the predicted theoretical mass loss (calculated by means of Faraday's law) can be found in Figure 8. The real mass loss will most probably be lower than this theoretical prediction due to for instance decreasing salt concentration, etc.

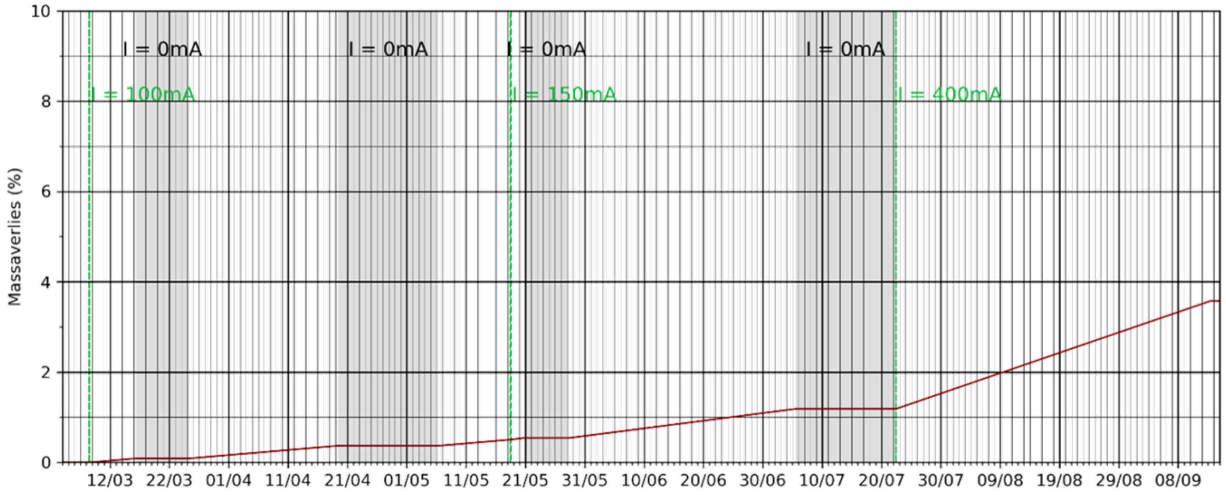

Figure 8. Predicted theoretical mass loss of the reinforcement during the corrosion experiment.

In order to expose only the longitudinal reinforcement between the bearings to the accelerated corrosion process, heat shrink tubes were installed around the reinforcement outside this area (see also Figure 7 (right)). Special heat shrink tubes with an internal adhesive coating were more-over used to prevent any seepage between the heat shrink tubes and the rebar.

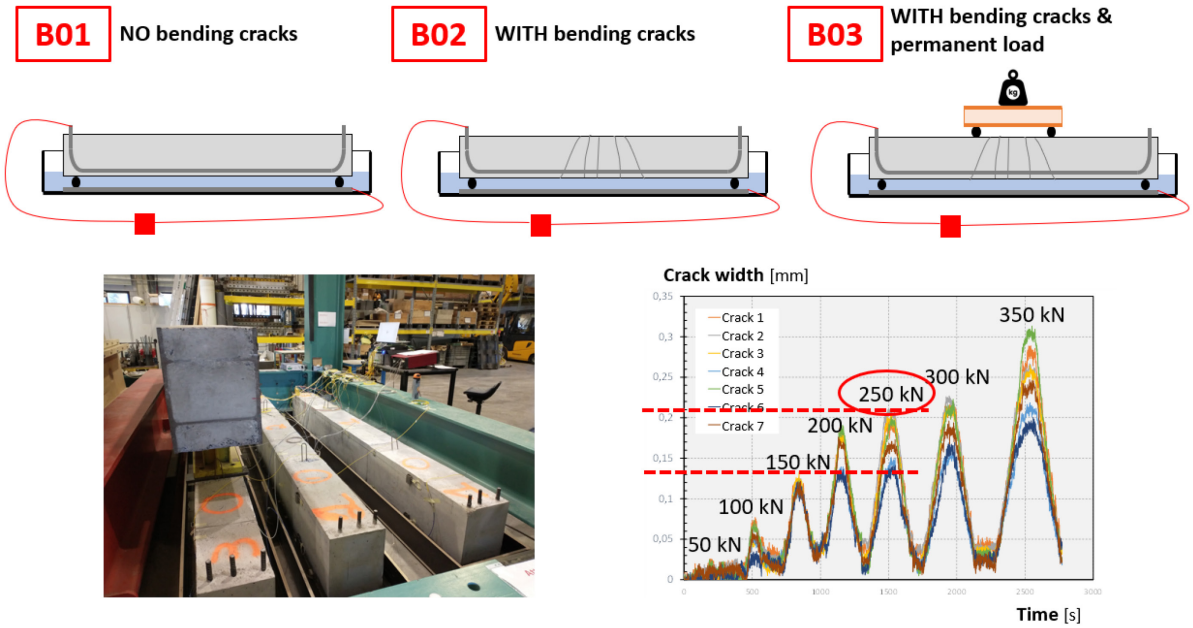

*Figure 9. The schematic representation and pictures of the experimental setup for the corrosion experiments. (right bottom) pre-cracking load and range of crack-widths (cf. reference beam experiment (see §**Error! Reference source not found.**1.2)).*

The 3 beams differ in pre-treatment (see also Figure 9). Beam B01 was placed in the salt bath without pre-loading. Beams B02 and B03 were first subjected to a pre-loading of 250 kN. Purpose of this preloading was to evaluate the impact of bending cracks on the corrosion process and whether this would be detected with the fibre optics. The pre-loading of 250 kN corresponds to an introduction of cracks with a crack width of 0.13 to 0.21 mm (see Figure 9). This crack width range is well below the durability requirement of 0.3 mm. This load level was determined based on the reference test performed on the 4th beam. After this pre-load, the cracks however close again. Consequently, a permanent load was placed on beam B03 to reopen the cracks. Because of practical constraints and safety considerations, only a limited permanent load of 25 kN could be placed on the beam. At the start of the corrosion process, the crack width of beam B03 was measured experimentally and was found to be approximately 0.04 mm.

During the accelerated corrosion process, more-over the beams were subjected to forced excitation dynamic tests during which the dynamic strains were measured with the internal and the external multiplexed FBG sensors. The aim was to monitor the modal characteristics that were identified from these dynamic tests, in order to investigate the influence of corrosion on natural frequencies and strain mode shapes.

1.4 Crack formation detection experiments

An additional set of validation experiments was performed in the framework of crack formation detection. For this purpose, steel fibre reinforced concrete beams of 150 x 150 x 900 mm³ were made in which mid span a notch of 25 mm was sawn (see Figure 11). Two types of BOFDA optical fibres were built in these beams, positioned at two heights above the saw cut (see Figure 10).

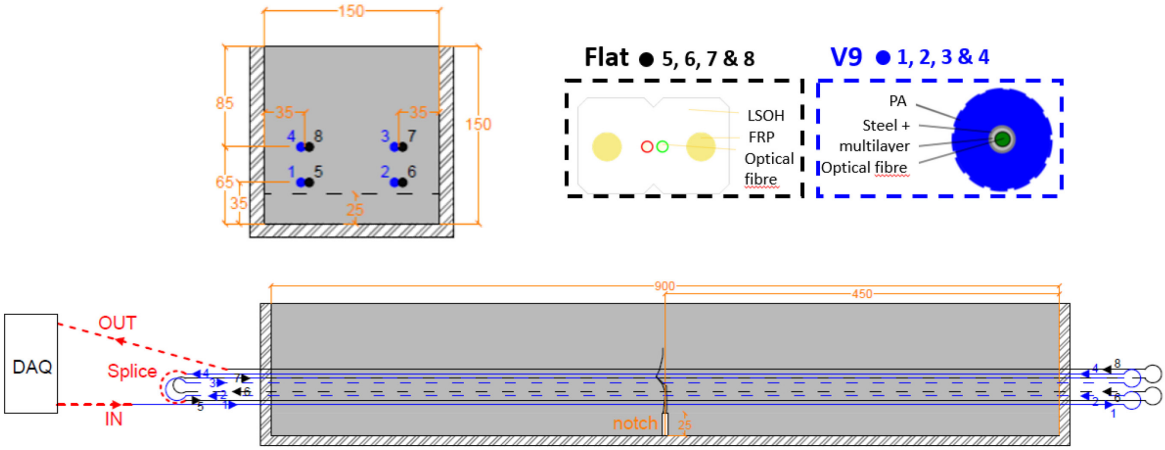

Figure 10. Optical fibre setup in the FRC beams.

These FRC beams were subjected to a 4-point bending test. Due to the presence of a local weakened section, one crack develops above the notch during the test. The test was executed in deflection control. During the experiment the displacement of the jack was stopped at different time interval to enable a BOFDA measurement, this at least twice, at a semi-constant strain situation. On one side of the specimen, crack development and, in particular, crack width evolution at the level of the BOFDA measurement lines were also monitored using Digital Image Correlation (DIC).

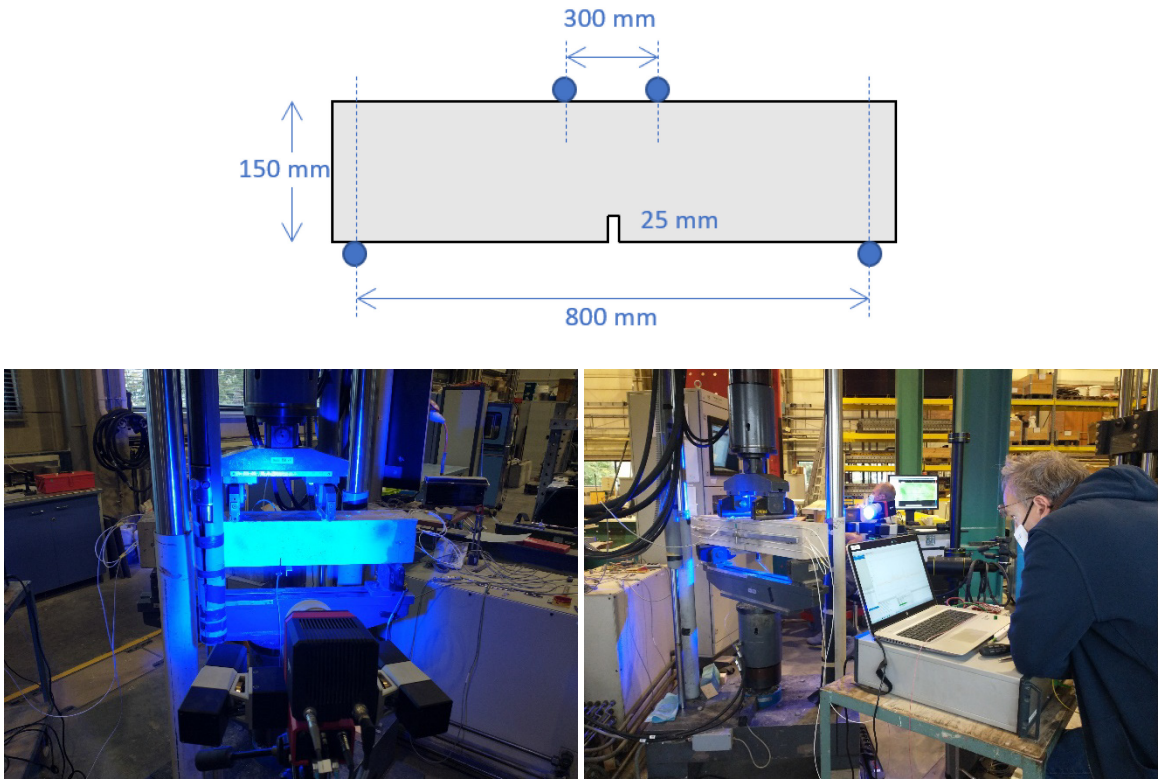

Figure 11. The experimental setup for the crack formation detection.

2 Reference beam experiments

2.1 Static results

In Figure 13, the results obtained with the FBGs mounted at the front of the beam (with centre-to-centre distance of the mounting blocks of 250 mm (spacing 220 mm)) are presented and compared with the DIC measurements at the different load steps. Due to the presence of the optical fibre lines on the surface, the DIC measurement is distorted in this area. The comparison was thus carried out based on the DIC measurements just below or just above the considered optical fibre measurement line (as illustrated in Figure 12 (top left)), which may lead to a slight deviation in absolute value between both measurements, nonetheless the general evolution can be evaluated and compared. For the DIC measurements, points were fixed to the surface at the ends of the mounting blocks (cf. free length of the optical fibre between the mounting blocks). At each load step, the distance change between these points was determined.

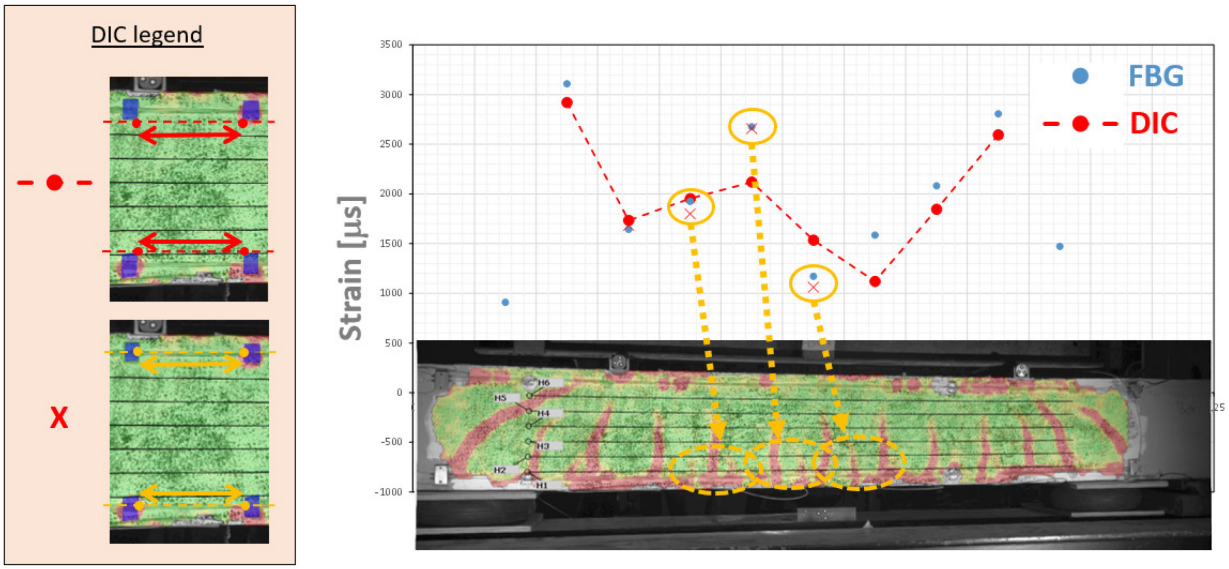

Figure 12. Results of FBGs mounted on the surface with extensometer length of 220 mm compared with equivalent DIC measurements at loading step 350 kN. (left) location of DIC measurements (right) location of smaller cracks at the bottom of the beam.

As can be seen in Figure 13, the results obtained with the FBG measurement lines show the same overall trend as those obtained with the DIC, especially at lower load steps. At higher loading, the FBG measurements sometimes deviate more strongly at the lower (tensile) side of the beam. However, upon further analysis, it can be seen in Figure 12 that these deviating values correspond to areas with smaller bending cracks (with a more limited height). Due to the shift in the DIC measurement line compared to the FBG measurement line, these are not registered with the DIC. An attempt was made to construct a DIC measurement line (where possible) at the height of the mounting blocks (see Figure 12 (bottom left)), these DIC measurements are shown by means of crosses in Figure 13. The latter show very good agreement with the FBG measurements even at higher load levels. This clearly illustrates that the FBG measurement line with a measurement base of 220 mm is well capable of detecting cracking.

(a)

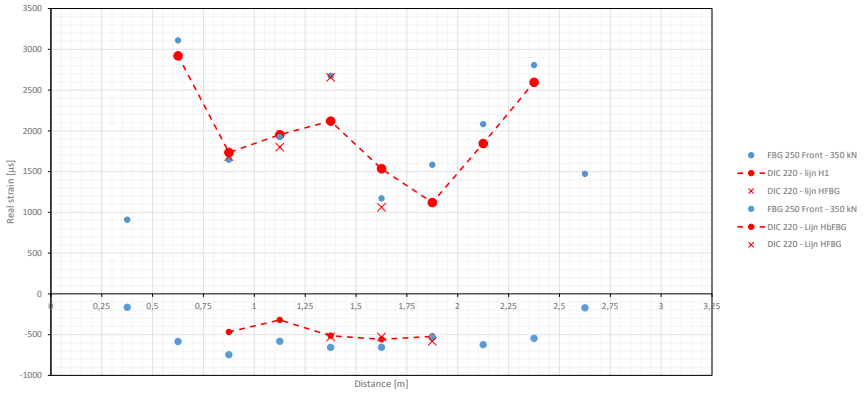
Real strain [µs]
Distance [m]
FBG 250 Front - 350 kN
DIC 220 - lijn H1
DIC 220 - lijn HFBG
FBG 250 Front - 350 kN
DIC 220 - Lijn HbFBG
DIC 220 - Lijn HFBG

(b)

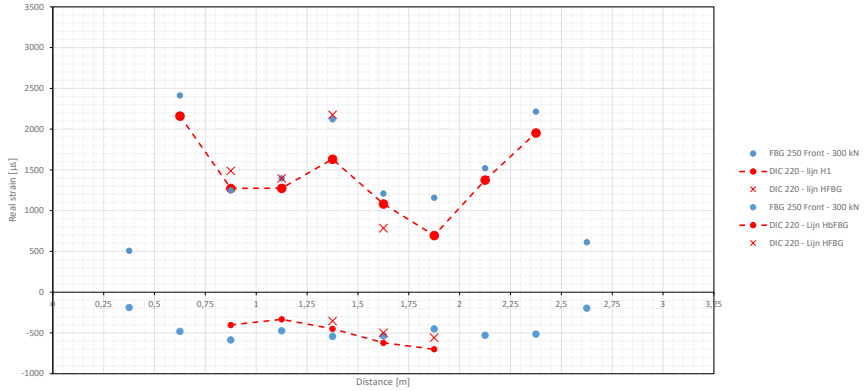
Real strain [µs]
Distance [m]
FBG 250 Front - 300 kN
DIC 220 - lijn H1
DIC 220 - lijn HFBG
FBG 250 Front - 300 kN
DIC 220 - Lijn HbFBG
DIC 220 - Lijn HFBG

(c)

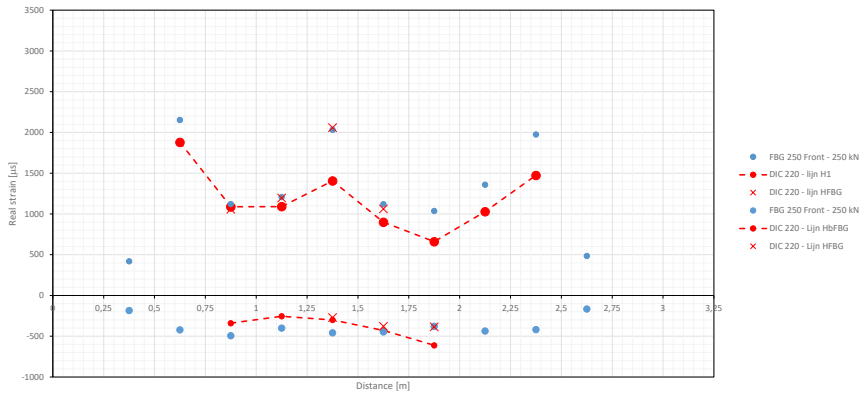
Real strain [µs]
Distance [m]
FBG 250 Front - 250 kN
DIC 220 - lijn H1
DIC 220 - lijn HFBG
FBG 250 Front - 250 kN
DIC 220 - Lijn HbFBG
DIC 220 - Lijn HFBG

(d)

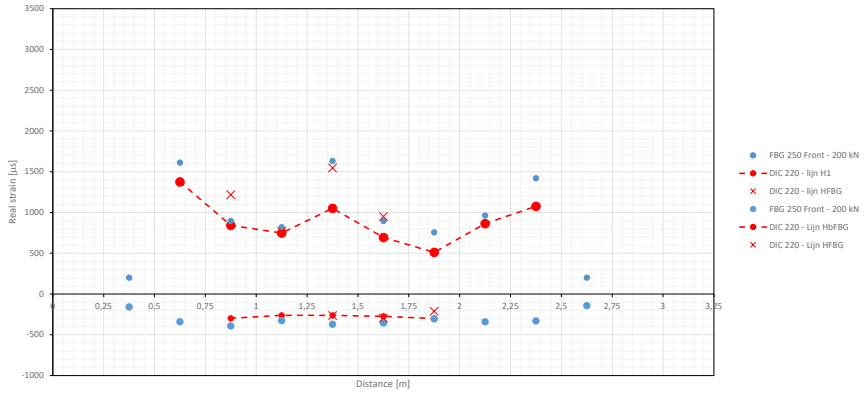
Real strain [µs]
Distance [m]
FBG 250 Front - 200 kN
DIC 220 - lijn H1
DIC 220 - lijn HFBG
FBG 250 Front - 200 kN
DIC 220 - Lijn HbFBG
DIC 220 - Lijn HFBG

(e)

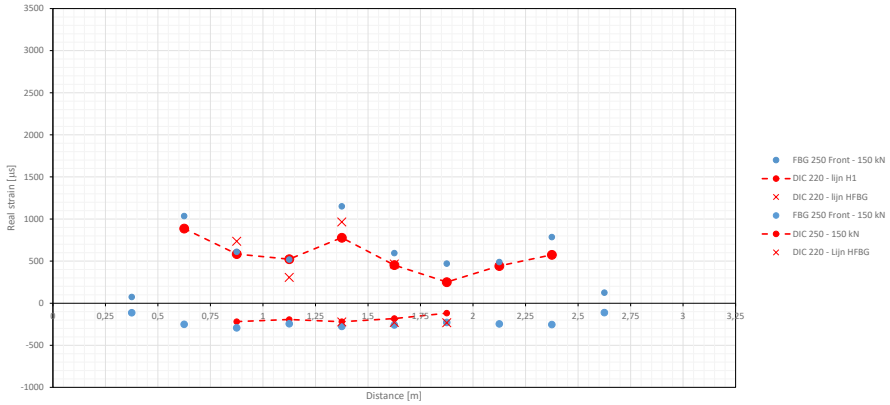

(f)

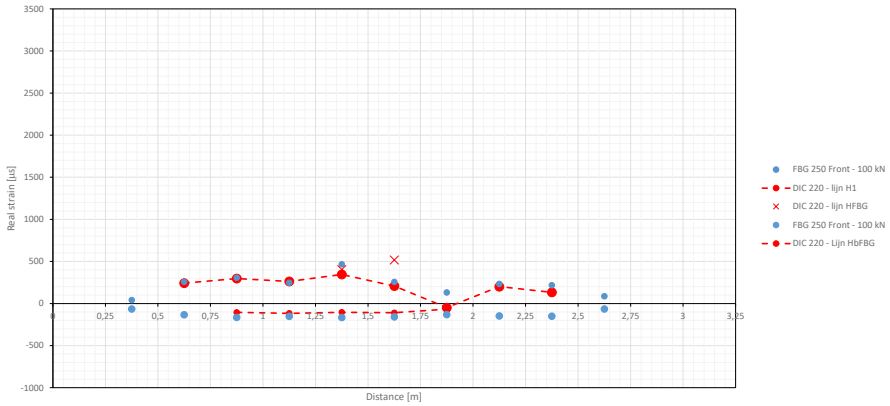

(g)

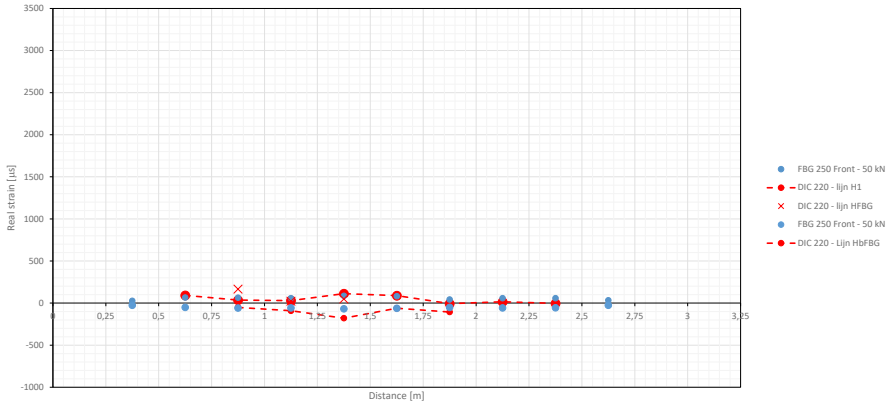

Figure 13. Results of FBGs mounted on the surface with extensometer length of 220 mm compared with equivalent DIC measurements.

In Figure 14, the results obtained with the FBGs mounted at the back of the beam (with centre-to-centre distance of the mounting blocks of 500 mm) are presented and compared with the DIC measurements and this at the different load steps. Again, a good agreement is obtained between the FBG and DIC measurements. There are nonetheless fewer outliers at higher loading, related to local cracks. This is logical since the measurements are performed over a larger area and thus the effect of one crack is smeared out.

(a)

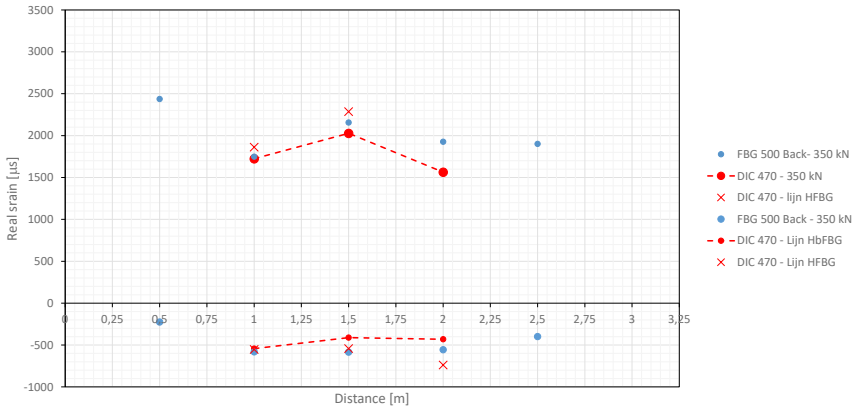
Real srain [µs]
Distance [m]
FBG 500 Back- 350 kN
DIC 470 - 350 kN
DIC 470 - lijn HFBG
FBG 500 Back - 350 kN
DIC 470 - Lijn HbFBG
DIC 470 - Lijn HFBG

(b)

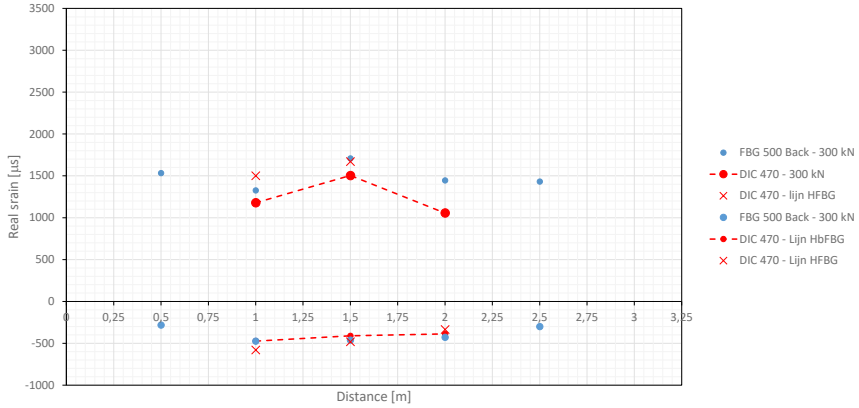
Real srain [µs]
Distance [m]
FBG 500 Back - 300 kN
DIC 470 - 300 kN
DIC 470 - lijn HFBG
FBG 500 Back - 300 kN
DIC 470 - Lijn HbFBG
DIC 470 - Lijn HFBG

(c)

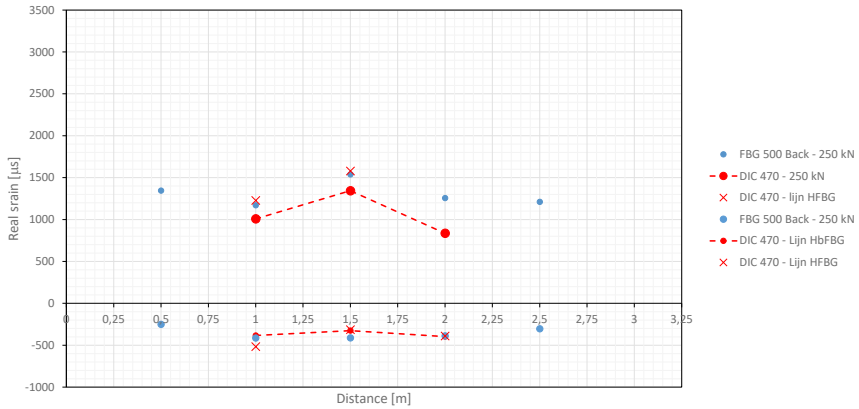
Real srain [µs]
Distance [m]
FBG 500 Back - 250 kN
DIC 470 - 250 kN
DIC 470 - lijn HFBG
FBG 500 Back - 250 kN
DIC 470 - Lijn HbFBG
DIC 470 - Lijn HFBG

(d)

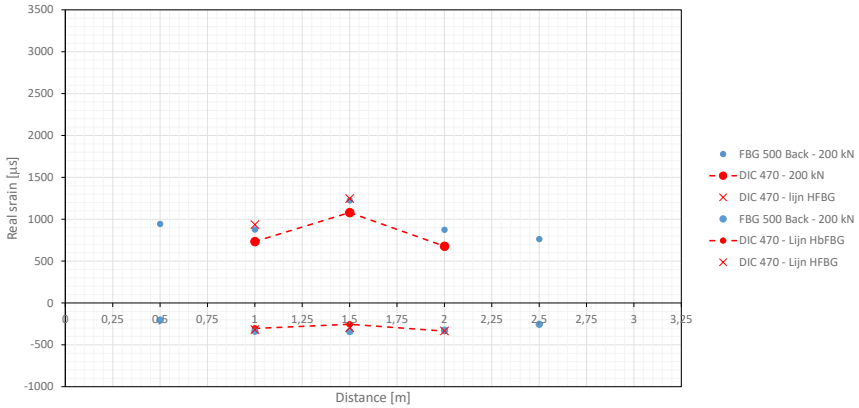
Real srain [µs]
Distance [m]
FBG 500 Back - 200 kN
DIC 470 - 200 kN
DIC 470 - lijn HFBG
FBG 500 Back - 200 kN
DIC 470 - Lijn HbFBG
DIC 470 - Lijn HFBG

(e)

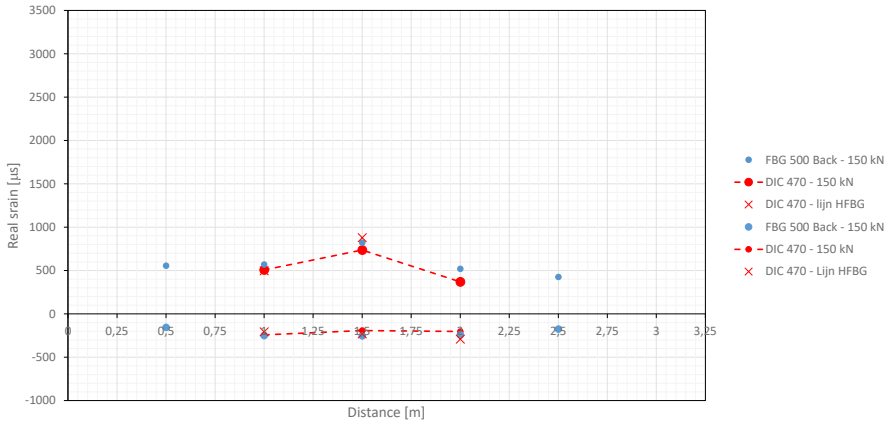

(f)

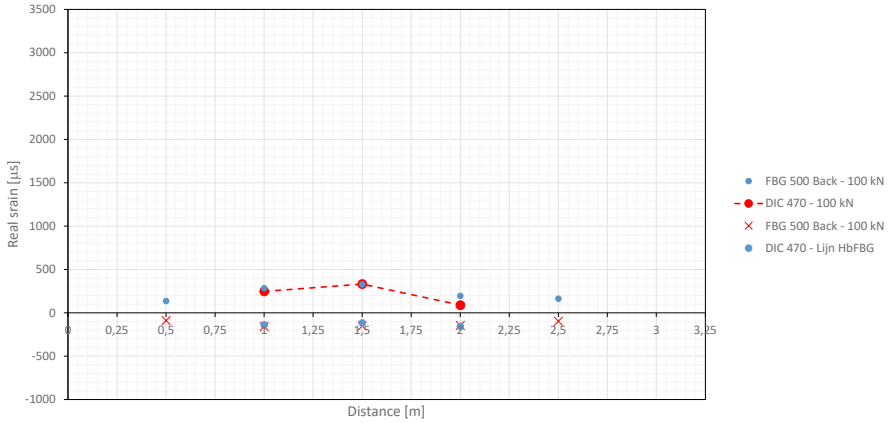

(g)

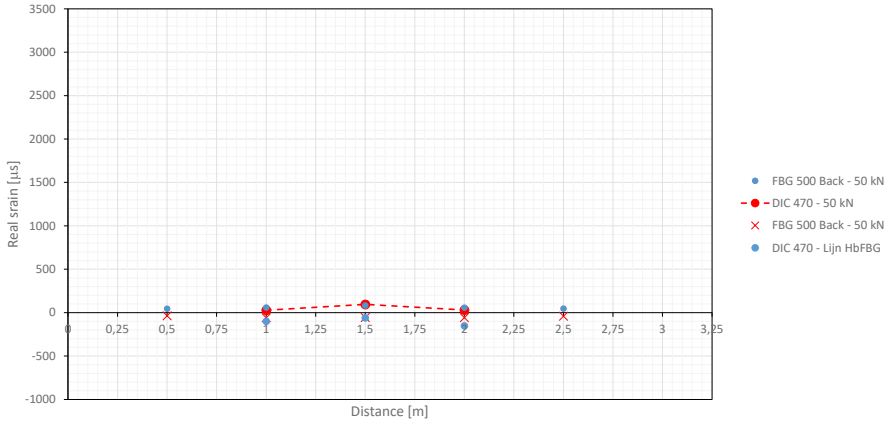

Figure 14. Results of FBGs mounted on the surface with extensometer length of 500 mm compared with equivalent DIC measurements.

When the results of the FBGs with a measurement bases of 250 and 500 mm are put side by side (see Figure 15), a very good agreement between the two sets of measurements can be observed. The results of the FBGs with a measurement base of 500 mm lie exactly between the 2 neighbouring FBGs with a measurement base of 250 mm.

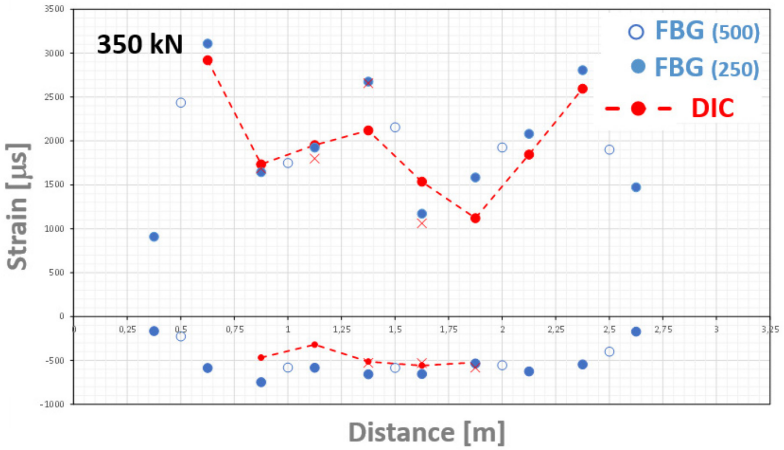

Figure 15. Results of FBGs mounted on the surface with extensometer length of 250 and 500 mm compared with equivalent DIC measurements (load step = 350 kN).

The results of the FBGs installed in the centre of the beam in semi-extensometer setup (with tubes of 300 mm placed around the carrier rod in which the FBG is glued) are presented and compared with the DIC measurements and this for the different load steps in Figure 16. Again, a good agreement is found with the DIC measurements.

(a)

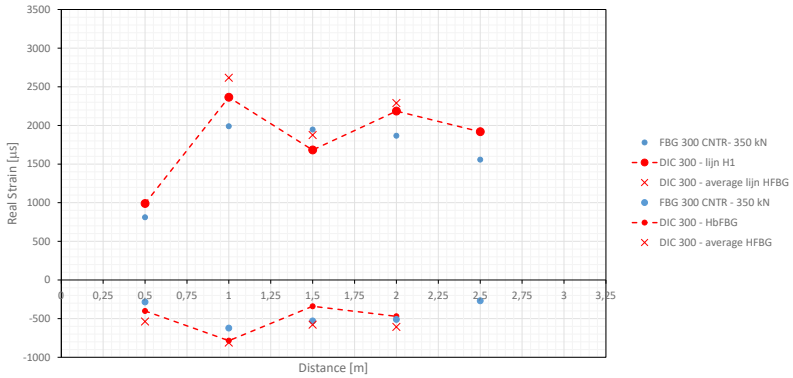

(b)

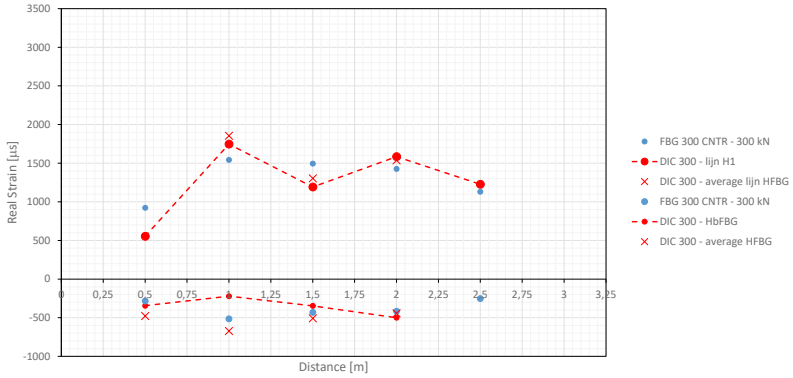

(c)

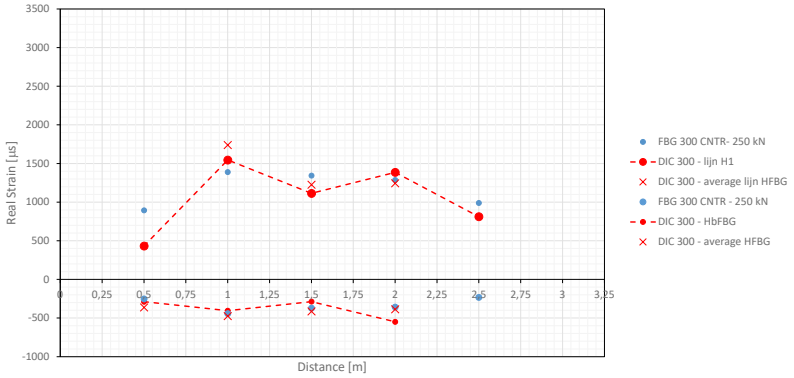

(d)

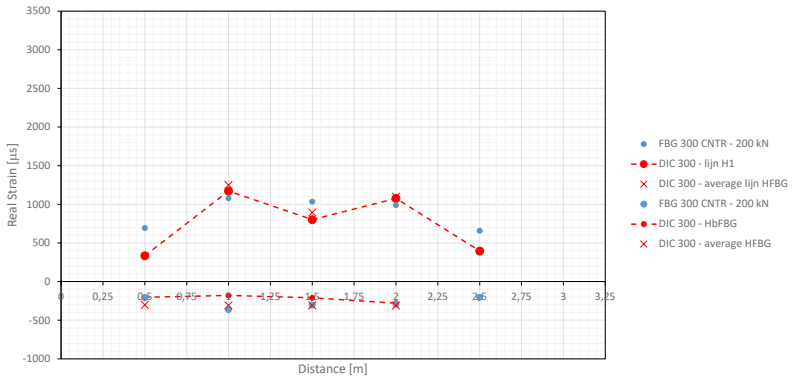

(e)

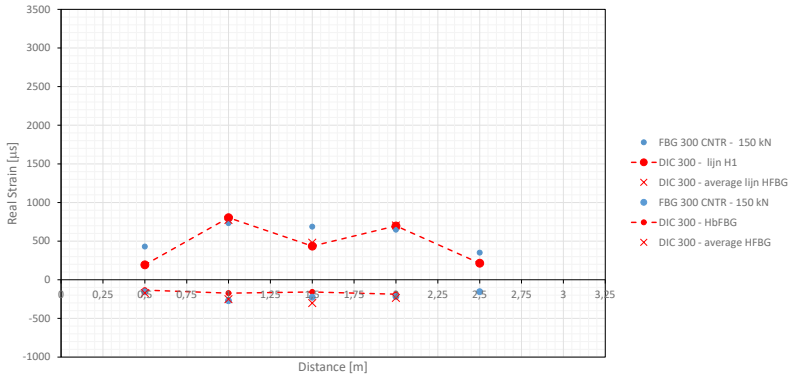

(f)

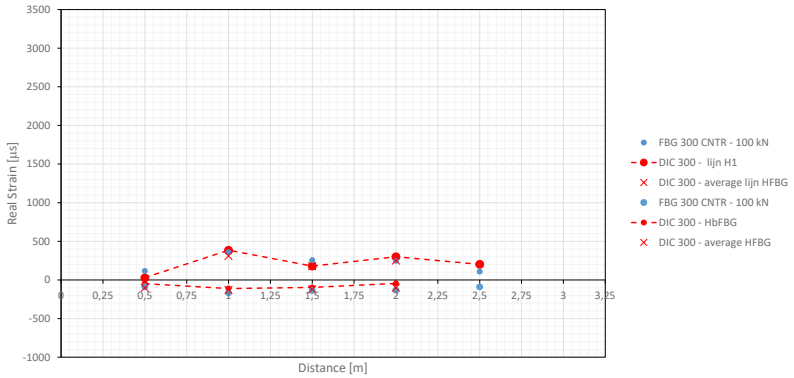

Figure 16. Results of FBGs installed in the center of the beam with a semi-extensometer setup (extensometer length of 300 mm) compared with equivalent DIC measurements.

When the results of the internal FBGs with semi-extensometer setup are compared with the externally mounted FBG measurement lines, also a good agreement is found with the external setup with a measurement base of 500 mm (see Figure 17). These results clearly show that the construction with the tubes acts as an extensometer, it remains however unclear solely based on these results what the actual measurement base is of this setup.

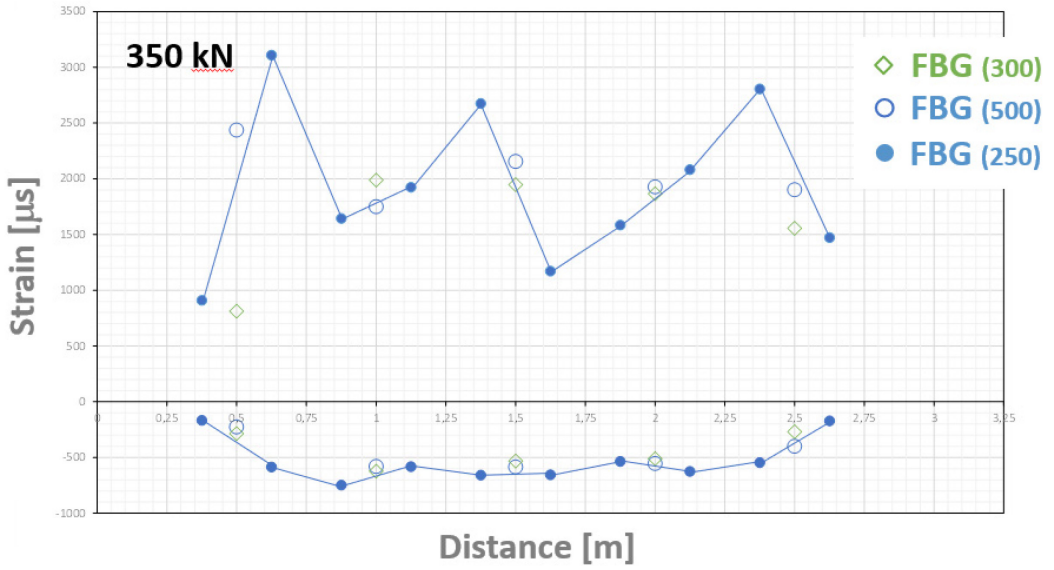

Figure 17. Results of FBGs mounted on the surface with extensometer length of 250 and 500 mm compared with semi-extensometer FBG setup installed in the concrete beam (load step = 350 kN).

The results of the FBG measuring line which was glued into the carrier rod (without tubing) can be found in Figure 18. In this figure, only the results of the FBGs in the tensile area of the beam are presented. These results are compared with the DIC measurements, therefor a line is constructed on the surface of the concrete just above the line of the mounting blocks. Along this DIC measuring line measuring points were attached to the surface of the beam with a spacing of 50 mm. The software then determined the length change between all successive measuring points. When these results are analysed in more detail, it can be clearly seen that the FBGs glued into the carrier rod register very local strains. The agreement with the DIC results is striking. Despite of its smooth surface, the carrier rod is thus well adhered to the concrete and consequently does not cause excessive smearing of the measuring zone of the FBG. The FBGs seem to exhibit a measurement base of around 50 mm with this setup. The latter also suggests that the semi-extensometer setup with tubes, discussed previously will most probably correspond to a extensometer with a base situated between 300 and 400 mm.

(a)

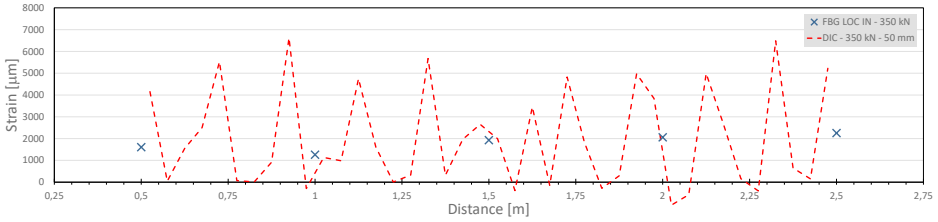

(b)

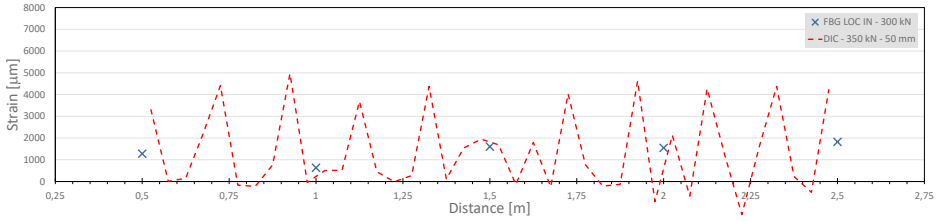

(c)

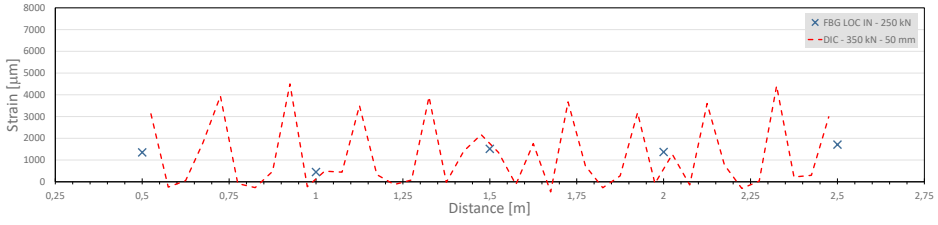

(d)

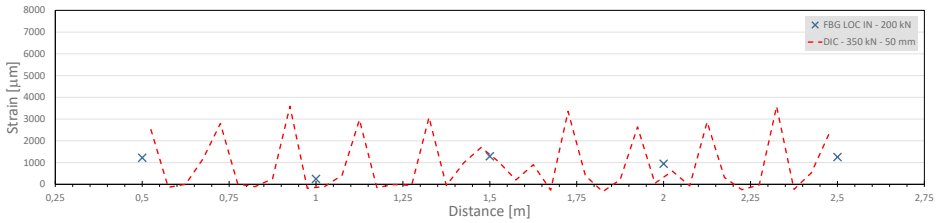

(e)

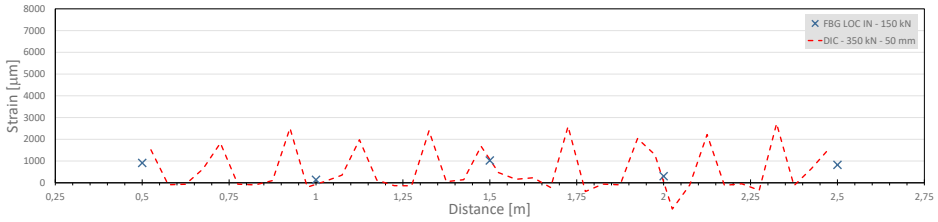

(f)

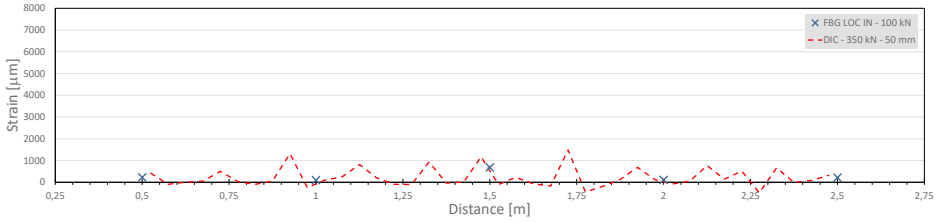

(g)

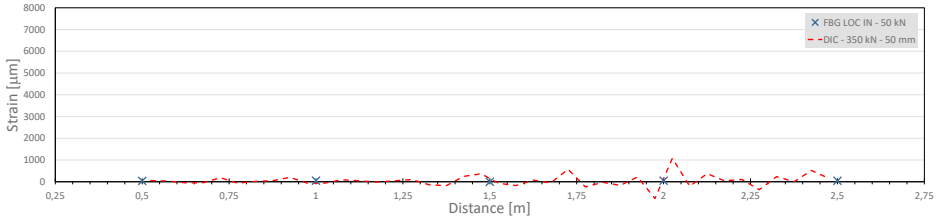

Figure 18. Results of FBGs installed at the bottom in the centre of the beam glued in a carrier rod compared with DIC measurements with a measurement base of 50 mm.

The results of the BOFDA measuring lines installed in the concrete were also compared with those obtained using the DIC. Early on it became clear that these results are much more complex to interpret. By way of illustration, in Figure 19 the BOFDA measurements obtained with the V9 measuring line located at the front in the concrete's tensile zone are presented. The utilised BOFDA measuring equipment provides measurement values every 50 mm along the optical fibre measuring line. Initially, these measured values were consequently compared with DIC measurements with a spacing of 50 mm (the software determines the length change between successive measuring points). In Figure 19(a) it can be clearly seen that the BOFDA measurement differs significantly from this DIC setup. The BOFDA is clearly not able to detect the individual cracks, presumably due to the dense crack pattern with a too limited spacing between the cracks. In a subsequent processing step, the BOFDA was assumed to provide a more smeared strain measurement. Consequently, the DIC measurement values obtained at an interval of 50 mm were averaged over various distances ranging from 200 mm to 500 mm (see Figure 19 (b) to (d)). The BOFDA measurements seem to show a good agreement with these averaged strains of the DIC. It is however difficult to state what the averaging of the BOFDA system is, and this might also differ from system to system.

(a)

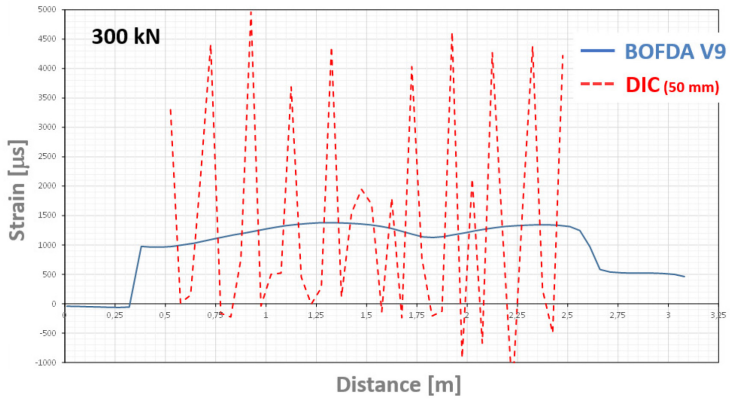

(b)

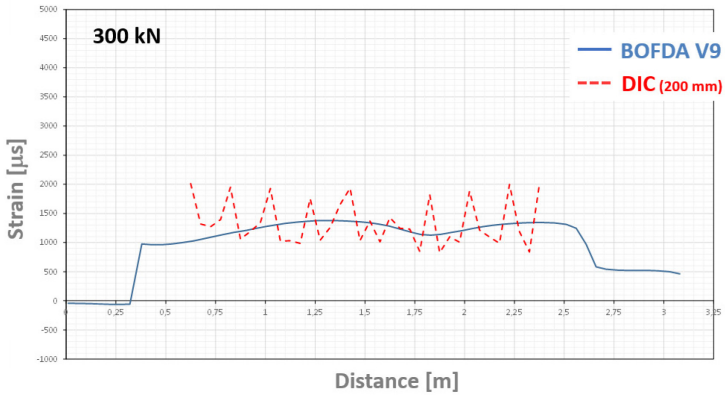

(c)

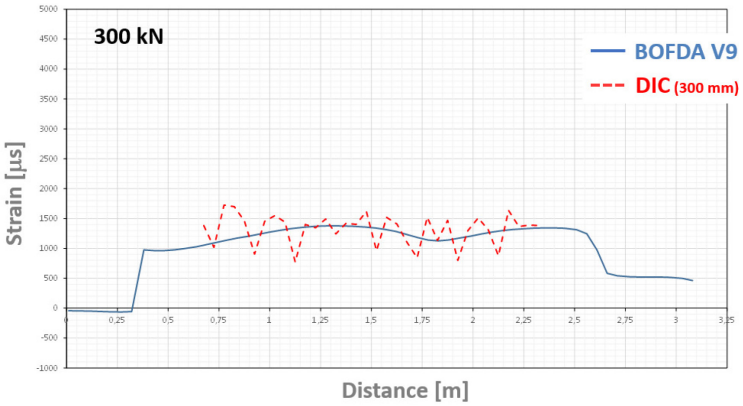

(d)

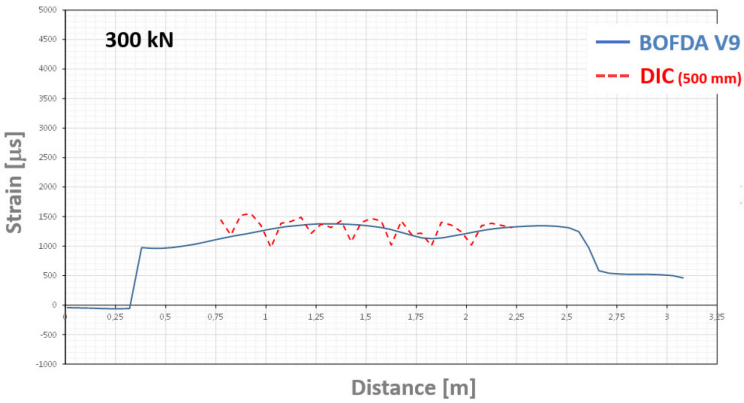

Figure 19. Results of BOFDA V9 installed in the concrete at the bottom on the front side compared with DIC measurements with a measurement base of 50 mm averaged over 0, 200, 300 and 500 mm.

Given that the DIC measurements are disturbed by the presence of the mounting blocks on the surface, several measurement lines at intermediate heights were constructed in the DIC software and the Euler-Bernouilli hypothesis was applied to determine the strains at the height of the BOFDA measurement lines with an averaging over 500 mm (see Figure 20). In Figure 21 and Figure 22 respectively, the comparisons of the DIC results with the ones obtained with the BOFDA V9 and Flat cable (situated at the front of the beam) can be found. Both show good agreement with the averaged DIC measurements. However, the BOFDA Flat measurement shows larger deviations at higher load levels. For both BOFDA types, a discrepancy is observed at the last load step, here, however, the suspicion arises that the Euler-Bernouilli hypothesis may no longer apply.

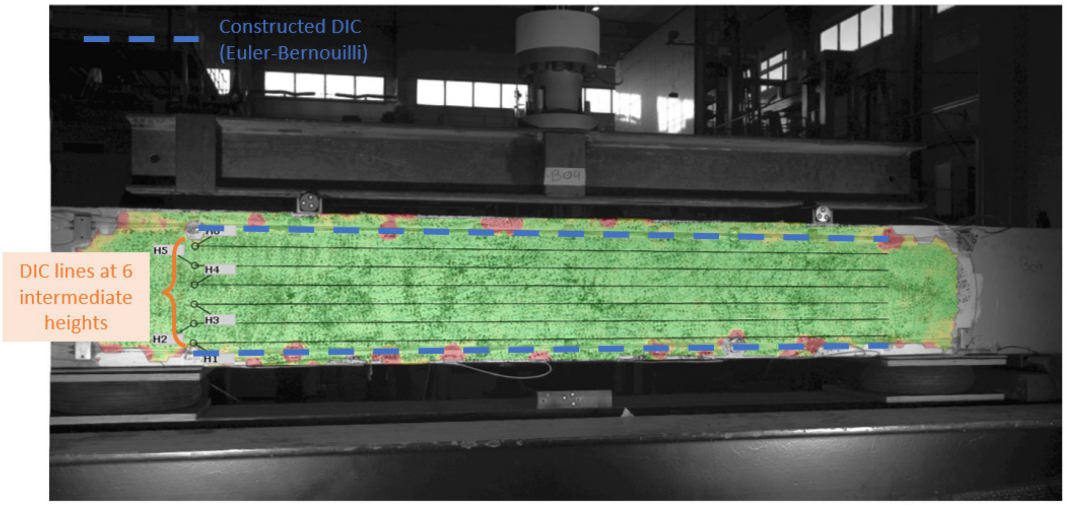

Figure 20. DIC data treatment with construction of measurement lines at intermediate heights and application of Euler-Bernouilli.

The measurements performed at the front and rear of the beam with the BOFDA V9 and BOFDA Flat were also compared with each other. This comparison at some of the load steps (150 and 300 kN) can be found in Figure 23. Similar profiles are observed at the front and rear. However, some peaks are more pronounced on one of the sides, as can be particularly well seen at the load step of 150 kN. Both BOFDA types however show a similar difference, which seems to point to a physical cause, namely that the crack widths at the front and rear of the beam are different. Both types show sudden jumps in the measurements at higher load steps. For the BOFDA Flat, however, these occur slightly earlier (already at the load step of 200 kN, where this is present for the BOFDA V9 type from 250 kN onwards). This observation together with the larger deviations from the DIC measurements at higher load steps seems to indicate that the BOFDA Flat is less appropriate for monitoring of elements with larger expected crack widths.

(a)

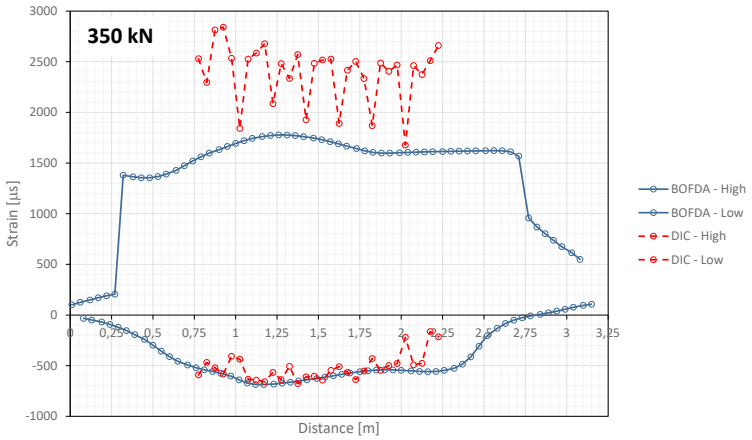
350 kN
Strain [µs]
Distance [m]
BOFDA - High
BOFDA - Low
DIC - High
DIC - Low

(b)

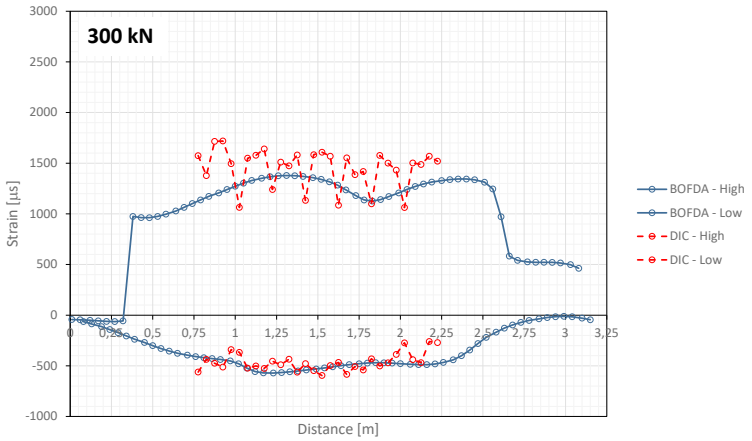
300 kN
Strain [µs]
Distance [m]
BOFDA - High
BOFDA - Low
DIC - High
DIC - Low

(c)

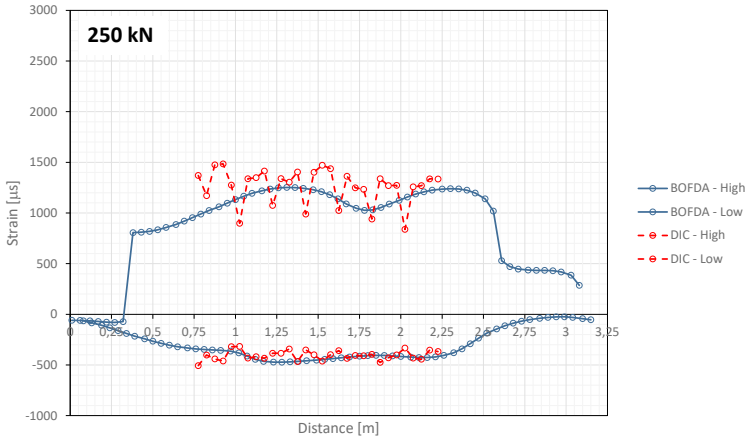
250 kN
Strain [µs]
Distance [m]
BOFDA - High
BOFDA - Low
DIC - High
DIC - Low

(d)

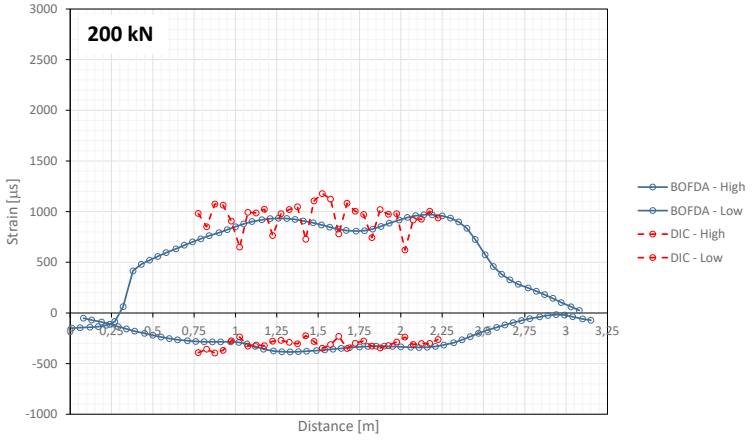
200 kN
Strain [µs]
Distance [m]
BOFDA - High
BOFDA - Low
DIC - High
DIC - Low

(e)

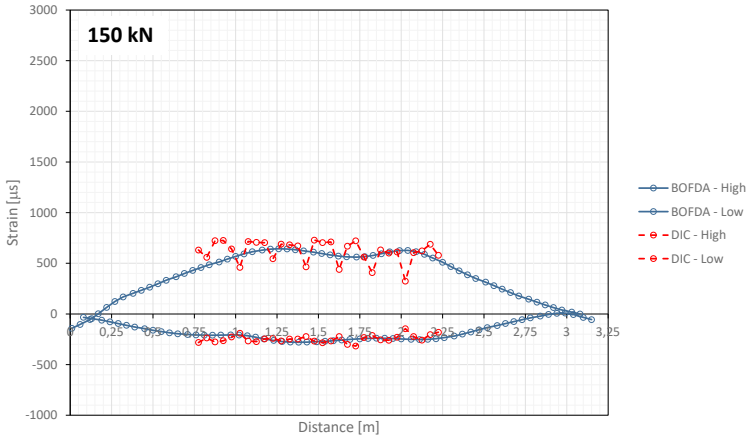

(f)

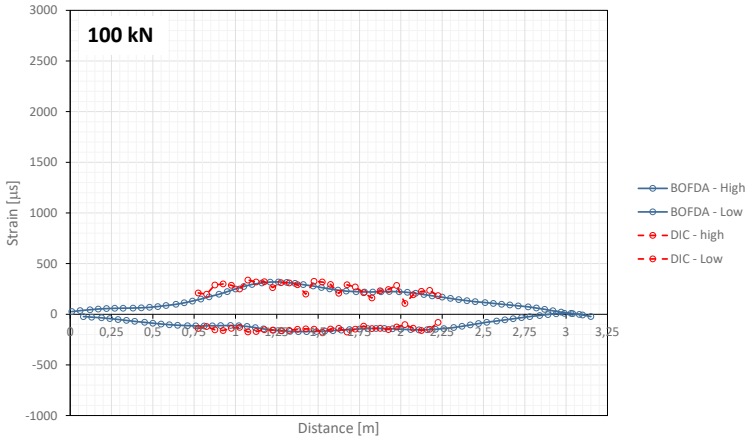

(g)

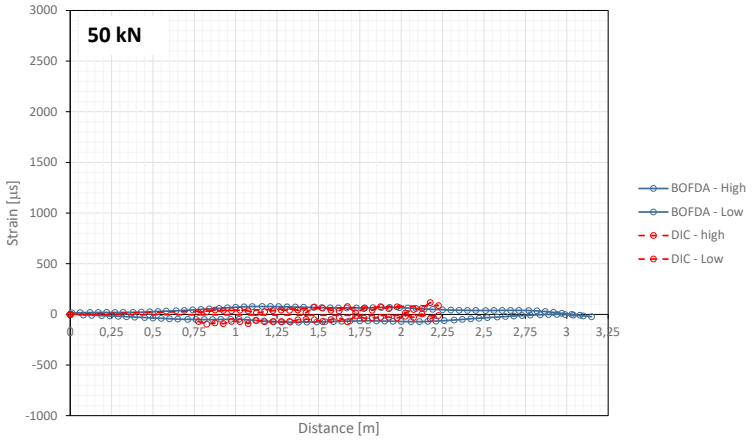

Figure 21. Results of BOFDA V9 installed in the concrete at the bottom on the front side compared with DIC measurements with a measurement base of 50 mm averaged over 500 mm and application of Euler-Bernouilli.

(a)

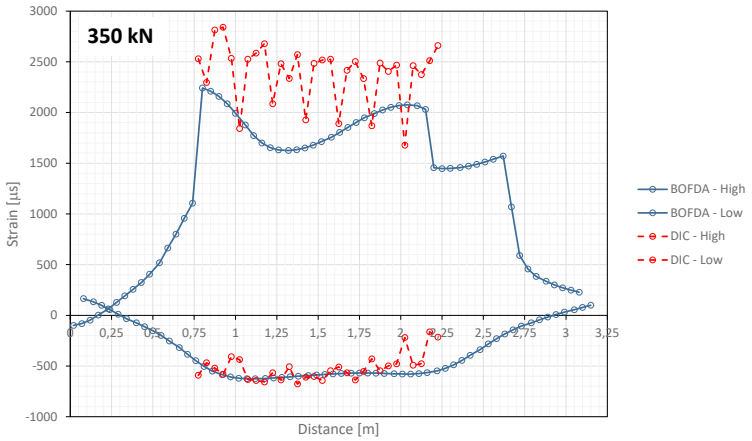
350 kN
Strain [µs]
Distance [m]
BOFDA - High
BOFDA - Low
DIC - High
DIC - Low

(b)

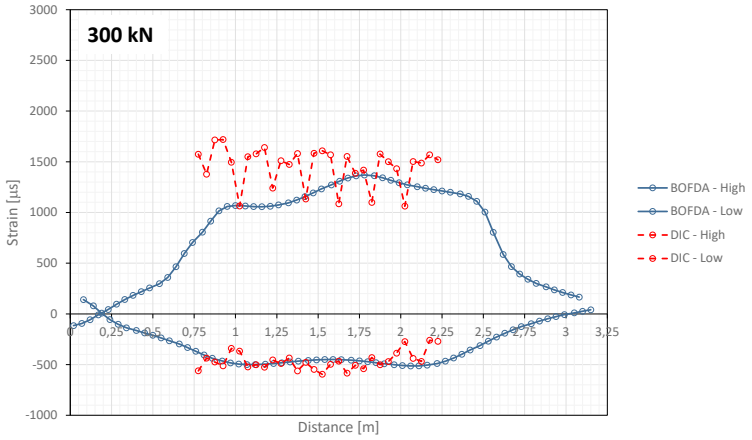
300 kN
Strain [µs]
Distance [m]
BOFDA - High
BOFDA - Low
DIC - High
DIC - Low

(c)

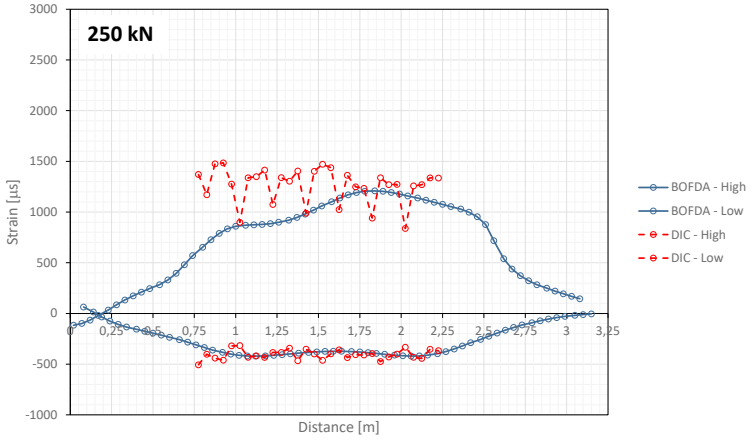
250 kN
Strain [µs]
Distance [m]
BOFDA - High
BOFDA - Low
DIC - High
DIC - Low

(d)

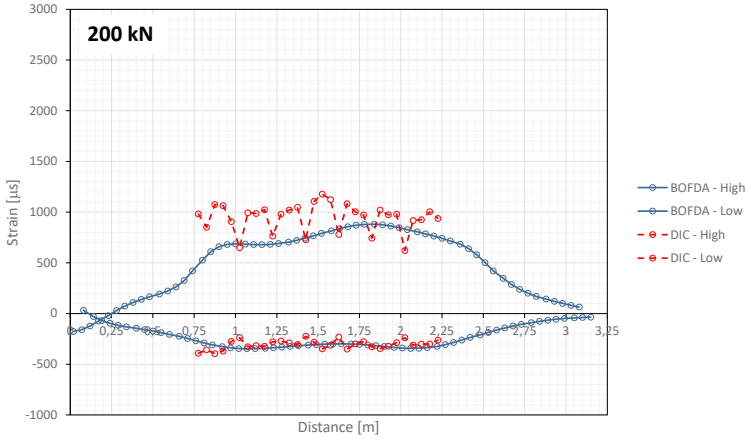
200 kN
Strain [µs]
Distance [m]
BOFDA - High
BOFDA - Low
DIC - High
DIC - Low

(e)

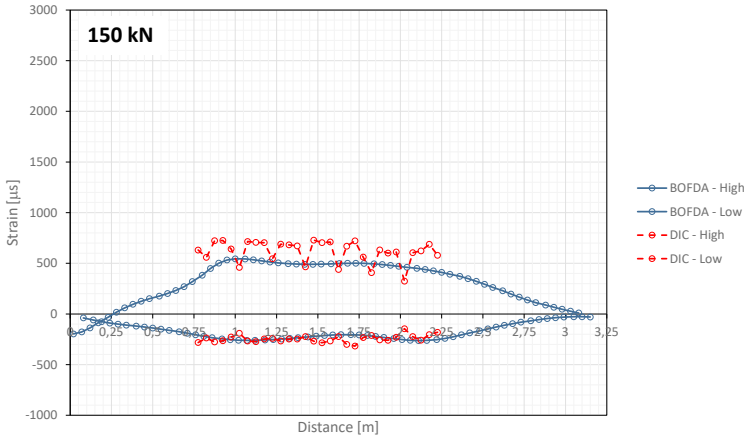

(f)

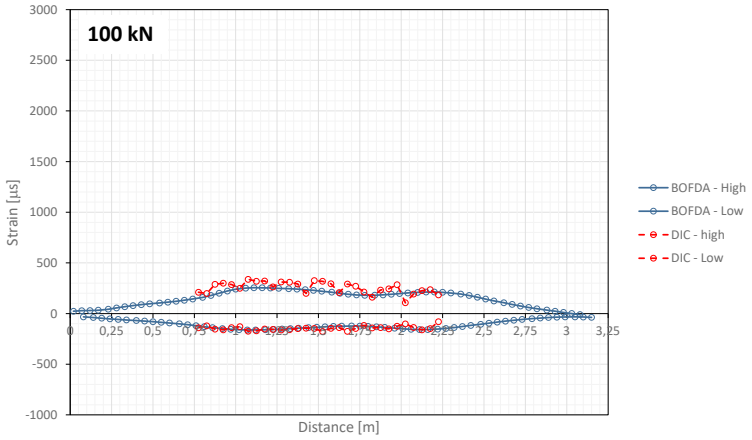

(g)

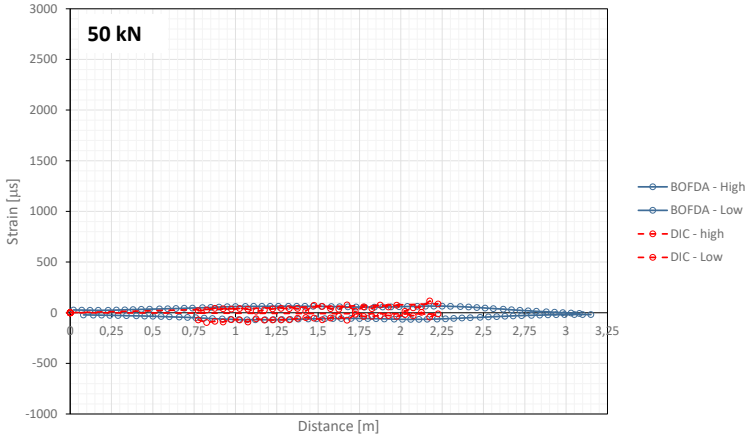

Figure 22. Results of BOFDA Flat installed in the concrete at the bottom on the front side compared with DIC measurements with a measurement base of 50 mm averaged over 500 mm and application of Euler-Bernouilli.

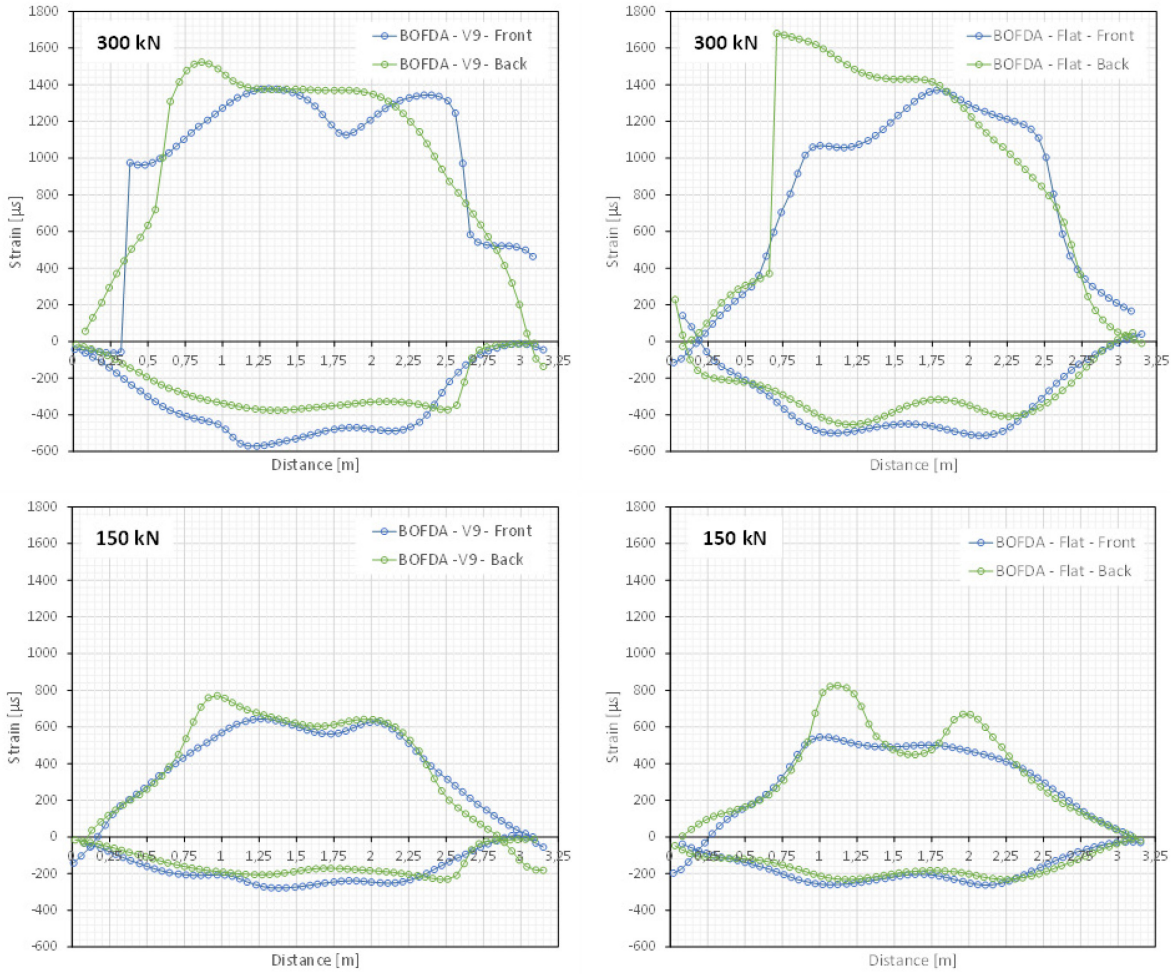

Figure 23. Results of BOFDA V9 and Flat installed in the concrete at the front and back side of the beam;

2.2 Dynamic results

As mention earlier after each loading step the beam was unloaded and placed on inflated tiers to create free boundary conditions in order to conduct a dynamic test. The dynamic strain data that are obtained from the FBG sensors mounted on the surface of the beam at the front and back of the beam are used for identifying the modal characteristics of the beam. Four beam modes are identified for the undamaged beam and after each loading cycle: the first and the second vertical bending mode and the first and the second lateral bending mode (Figure 24). The influence of damage on the modal characteristics is investigated next.

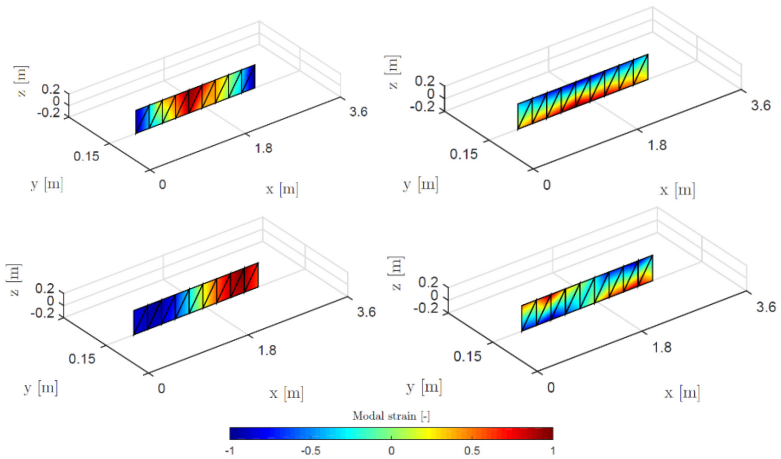

Figure 24. Strain mode shapes of the first four modes of the B04 beam (undamaged beam). Top left: first lateral bending mode (L1), f=88.3Hz. Top right: first vertical bending mode (B1), f=117.1 Hz. Bottom left: second lateral bending mode (L2), f=236.2 Hz. Bottom right: second vertical bending mode (B2), f=301.8 Hz.

The evolution of the natural frequencies of the first four bending modes throughout the progressive damage test (PDT) is displayed in Figure 25. The natural frequencies gradually decrease with increasing level of damage. The maximum relative reduction of the natural frequency values is about 12% for all modes, at the end of the final loading cycle (loading amplitude of 350 kN), showing a clear influence of damage on natural frequencies. It is interesting to notice that even after the first loading cycle, when the cracking load for macro-cracks of the concrete was not exceeded, a relative reduction of about 1% was already observed on the natural frequencies presumably due to the formation of the first micro-cracks in the concrete matrix.

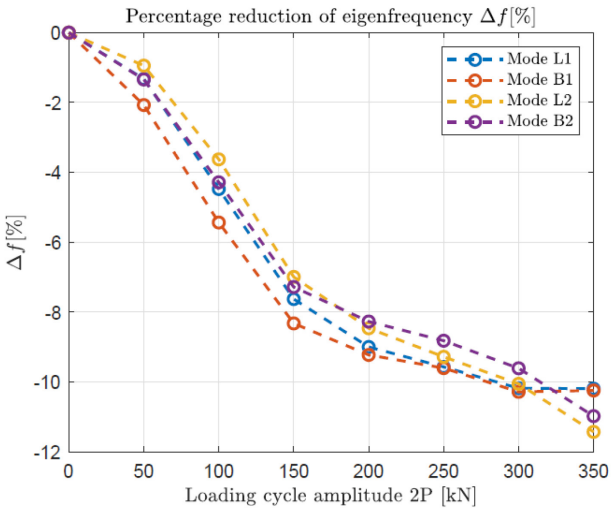

Figure 25. Relative eigenfrequency difference of the four identified modes of the B04 beam for the different steps of the progressive damage test.

A clear influence of the damage on the strain mode shapes of the identified modes can be observed, already after the first loading cycle. As a representative example, the strain mode shape of mode B1 is given in Figure 26, as obtained from the side of the beam that is equipped with 10 FBG sensors (5 at the top and 5 at the bottom, with a spacing of 500 mm). A clear reduction of the modal strain amplitude at the top and an increase at the bottom is observed as the PDT progresses. This behavior can be explained by the type of damage (bending cracks) that is introduced in the beam, which results in a redistribution of the strains in the beam and a corresponding shift of its neutral axis towards the undamaged zone[1]. This shift of the neutral axis can be also quantified (Figure 27), based on the identified strain mode shapes[1].

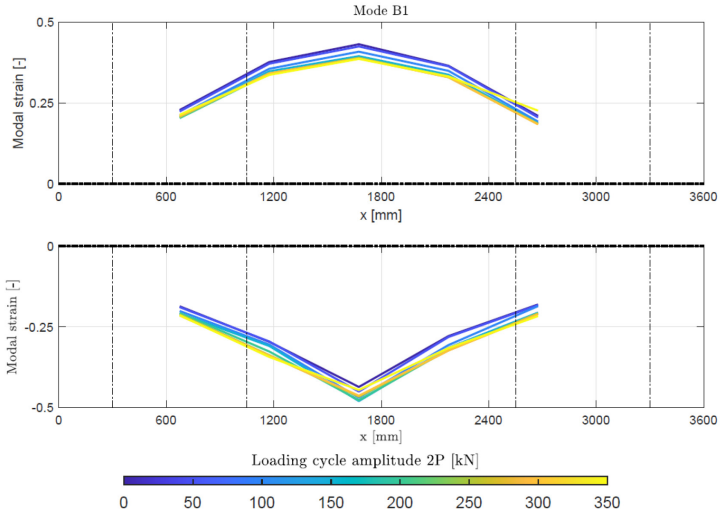

Figure 26. Strain mode shapes that have been identified after each loading-unloading cycle of the progressive damage test for mode B1. The top and bottom subplots contain the strains at the top and bottom of the beam respectively.

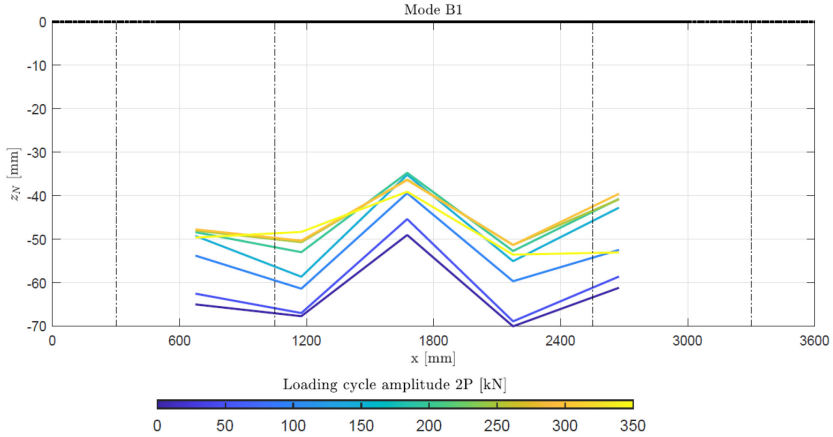

Figure 27. Neutral axis positions (z_N) that have been identified after each loading-unloading cycle of the progressive damage test from mode B1, with respect to the center of gravity of the beam (z_N=0 mm).

[1] D. Anastasopoulos, G. De Roeck, and E. P. B. Reynders, "Influence of damage versus temperature on modal strains and neutral axis positions of beam-like structures," *Mechanical Systems and Signal Processing,* vol. 134, 2019.

3 Results of Corrosion experiments

3.1 Static results

The optical fibre measurement lines attached to the concrete surface of the 3 specimens were partially detached during the duration of the corrosion test. The mounting blocks were only glued to the concrete surface. During the accelerated corrosion experiment the growth of corrosion products as well as deposition of salts revealed very harmful for this fixation principle, as some of the mounting blocks loosened during the test. Consequently, for long-term monitoring campaigns, an additional mechanical fixation was found to be necessary.

The internal measuring lines survived the accelerated corrosion test without any problems. In what follows, we will therefore only elaborate on these results. We will start with the semi-extensometer FBG setup, which proved to be very performant in the static reference test. Also for the accelerated corrosion test, these measurement lines provide very interesting results. In Figure 28 the results of these FBGs are shown as a function of time, grouped per beam. The strain on the compression side (top side of the beam) are quite similar for the 3 beams. However, a clear difference can be observed between the results of the 3 beams on the tensile side (underside of the beam, exposed to the corrosion conditions) and this already from the start of the accelerated corrosion test. In the tensile zone, beam B01 shows the lowest and beam B03 the highest tensile strains. Beam B02 is located somewhere in between these two. Zooming in on the start of the accelerated corrosion test, it can be seen that the results of beams B01 and B02 increase more-or-less equally until the end of October, after which the tensile strains of beam B02 start to increase more strongly. Beam B03 already shows higher tensile strains from the start of the accelerated corrosion test.

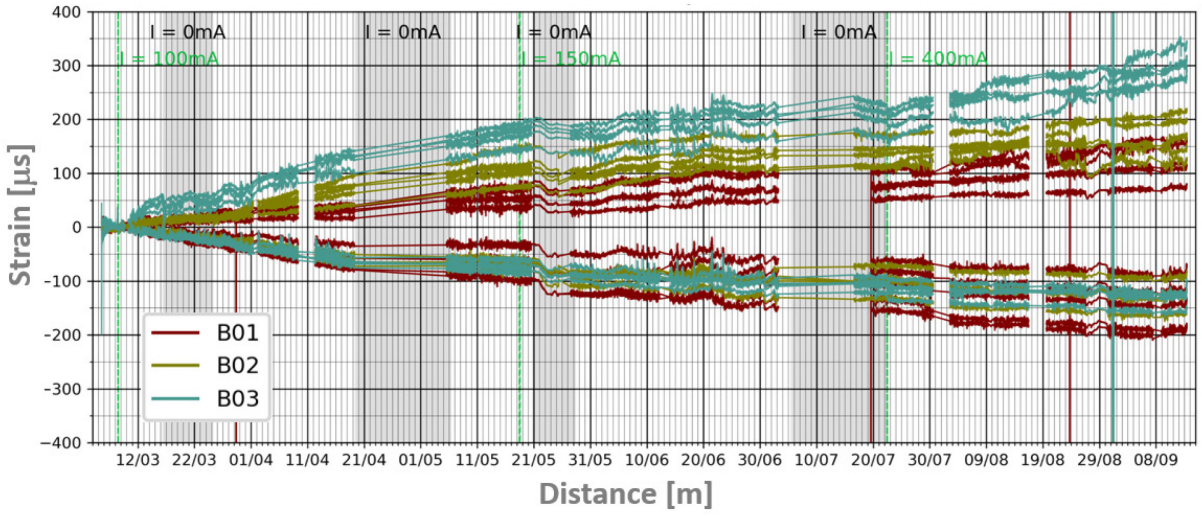

Figure 28. Results of FBGs installed in the center of the beam with a semi-extensometer setup and this for the 3 beams exposed to the accelerated corrosion experiment.

Although generally the results of beam B01, B02 and B03 agree with expectations, i.e. that beams B02 and B03 will potentially corrode more/ faster due to the presence of (open/closed) cracks, the measured

tensile strains are much higher than expected. A finite element model was constructed in DIANA to determine the expected strains for the calculated theoretical mass loss (taking into account creep effects and degradation of the concrete) (cf. Annexe 1). This FEM modelling yielded significantly lower tensile strains than those measured during the test. It is therefore possible that other phenomena influence the measurement, e.g. lateral growth of corrosion products and growth of splitting cracks, moisture absorption by the optical fibres, chemical deterioration of the glass fibre, etc. More research is needed to clarify this. Despite these unknowns, it can nonetheless be concluded that optical fibres can be useful in the context of corrosion monitoring.

The same general trend was also observed with the BOFDA measurement lines (see Figure 29 and Figure 30), however, also due to the inherent averaging of the BOFDA optical fibre measurement technique, the differences observed between the inter-beam results are much less pronounced (certainly between B01 and B02).

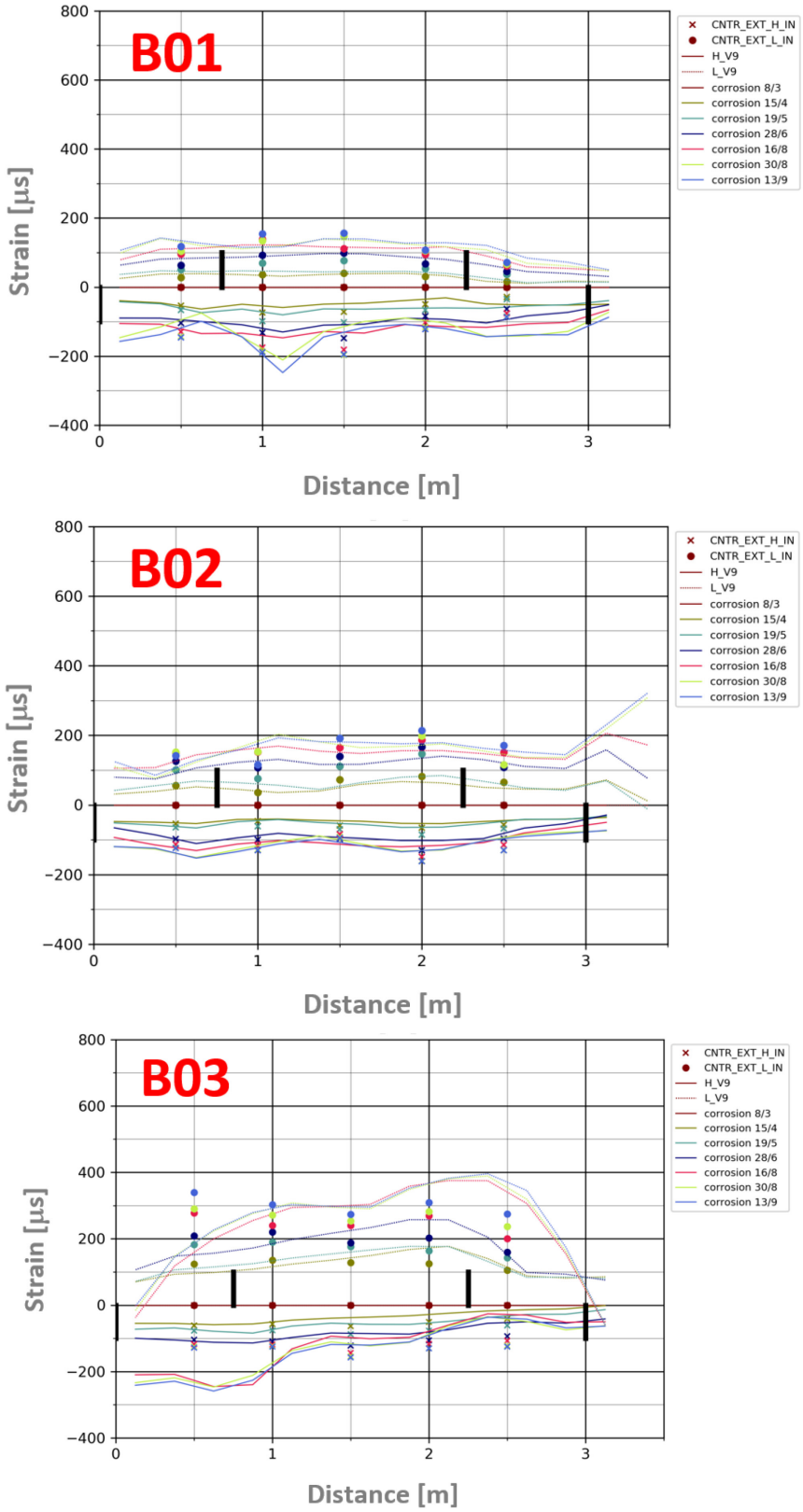

Figure 29. Results of the FBGs (semi-extensometer setup) and BOFDA's V9 (average of front and back lines, averaged over a distance of 0,25 m) installed in the beam. For the 3 beams at 7 selected corrosion durations.

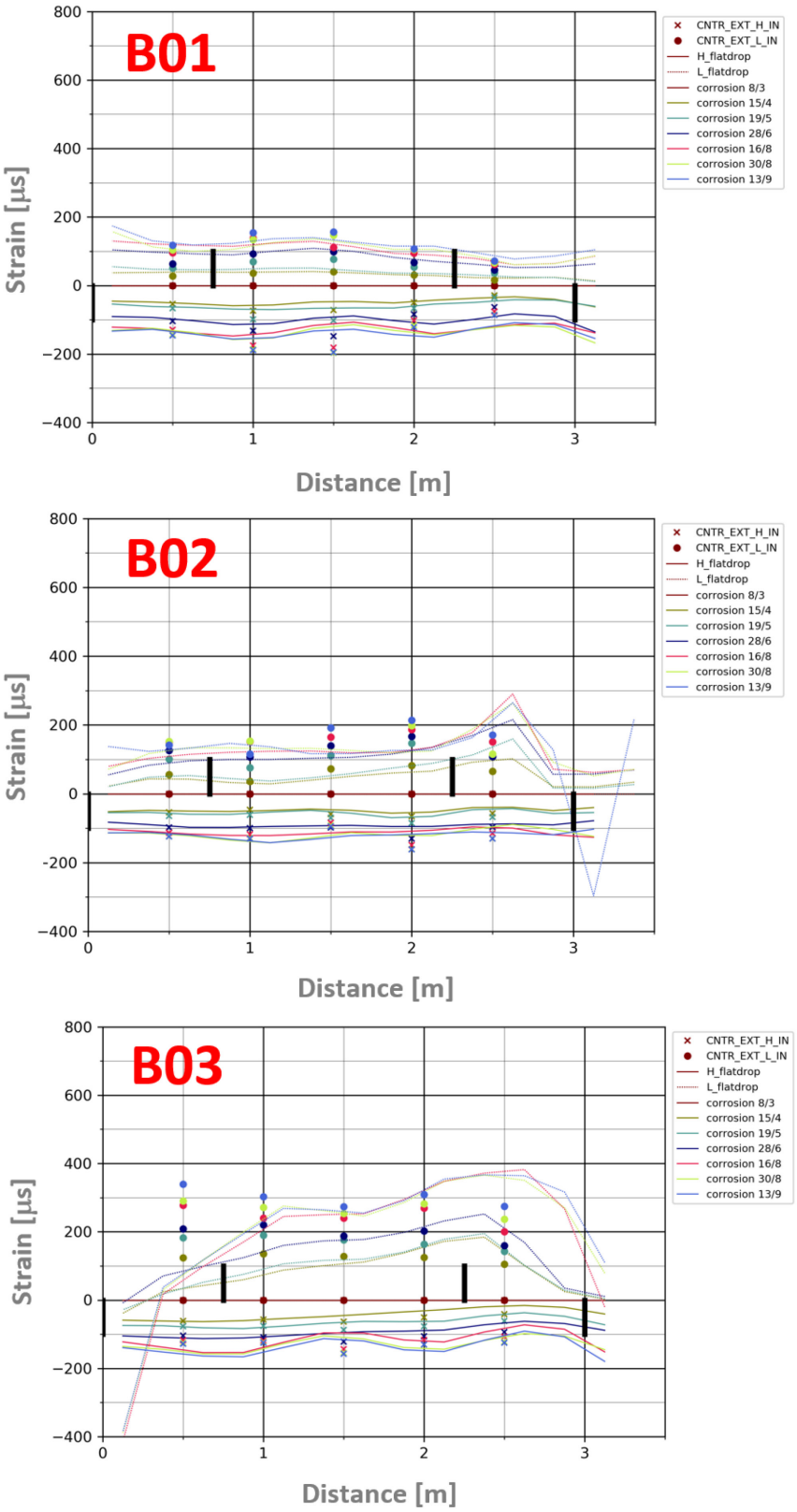

Figure 30. Results of the FBGs (semi-extensometer setup) and BOFDA's Flatdrop (average of front and back lines, averaged over a distance of 0,25 m) installed in the beam. For the 3 beams at 7 selected corrosion durations.

When analyzing the results of the FBGs that were only bonded in the support rod (local setup) a much stronger spread is present on the measurement results (in the tensile area, see Figure 31). That again confirms that we perform a very punctual measurement with this setup and moreover due to the presence of the cracks in beam B03 localized phenomena occur (e.g. corrosion on the one hand and possibly also water absorption on the other hand).

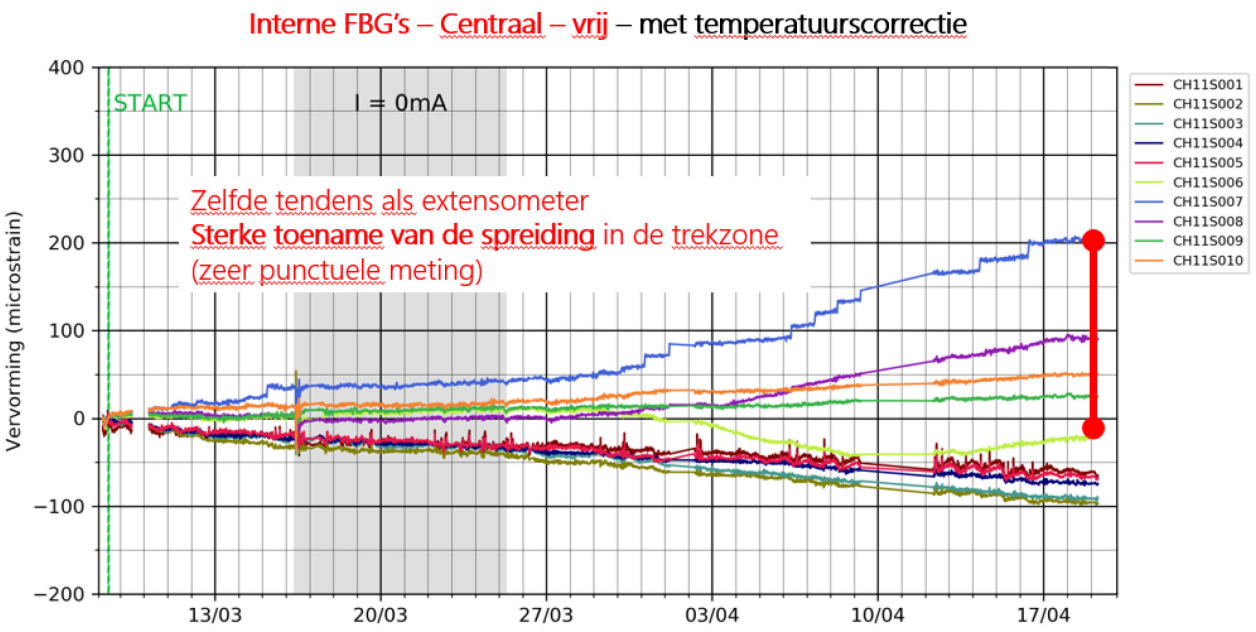

Figure 31. Results of FBGs installed in the center of the beam with a local setup (beam B03) exposed to the accelerated corrosion experiment.

At the end of the accelerated corrosion experiments, core drillings were carried out at the level of the point loads. In Figure 33 some pictures of one of these core drillings can be found, which was carried out at the level of the lower longitudinal reinforcements. It clearly shows the extensive network of splitting cracks and the deposition of corrosion products in these cracks. The optical fibre measuring lines are also visible. Based on this core, it becomes clear that the internal FBG sensors, which were provided in an extensometer setup, are located just at the level of a large splitting crack which connects the 3 rebars and moreover is characterised by a large crack width. The BOFDA measuring lines are located above the corner reinforcements and are thus less impacted by these splitting cracks. This might partly confirm the hypothesis made earlier, namely that the optical fibres are also influence by other phenomena besides mass loss.

(a)

(b)

Figure 32. Pictures of the bottom rebars after the accelerated corrosion experiment: (a) top view and (b) bottom view.

Figure 33. Pictures of a core drilling executed in beam B02 at the level of one of the point loads at the height of the lower longitudinal rebars.

When looking at the bottom rebar collected out of the beam B02 (between the two point loads) after the accelerated corrosion experiment, see Figure 32, one can clearly see that de top of the rebars are only locally corroded, probably linked to the locations of larger bending cracks. The bottom of the rebar is more uniformly corroded.

A photo of the crack surface of one of the splitting cracks can also be found in Figure 34. A significant deposition of corrosion products can be clearly seen in the splitting crack.

Figure 34. Picture of the crack surface of one of the splitting cracks of beam B02 after the accelerated corrosion experiment.

3.2 Dynamic results

As mentioned earlier during the accelerated corrosion process, the beams B01, B02 and B03 were subjected to forced excitation dynamic tests during which the dynamic strains were measured with the internal and the external multiplexed FBG sensors. The aim was to monitor the modal characteristics that were identified from these dynamic tests, in order to investigate the influence of corrosion on natural frequencies and strain mode shapes. However, the modal characteristics that were obtained from these tests could not be used for damage detection purposes because it was found that they were also influenced by several other external factors.

The most important external factor influencing the monitored modal characteristic consisted of changes in the static boundary conditions of the beams. The beams had to be removed multiple times from the baths in which they were placed, while the water level in the baths was also fluctuating during the corrosion process. This led to an inconsistency of the external boundary conditions among the different tests. Boundary conditions define the stiffness of the beams and consequently, their modal characteristics. Since the boundary conditions were changed and corrosion damage was introduced at

the same time, it was not possible to distinguish between both effects. This issue is less of a concern for full-size civil structures, as there the changes in the boundary conditions can be monitored separately.

Another factor that increased the uncertainty on the measured dynamic strains and consequently on the identified modal characteristics was the relatively low resolution of the acquisition unit employed during these tests, compared to the one that was used for acquiring the dynamic strains of B04. A very high accuracy and precision is required for low-amplitude dynamic strain measurements. Consequently, the relatively low resolution of the acquisition unit resulted in a relatively low accuracy of the identified the strain mode shapes of the beam. As a result, the ability to identify damage related changes on the strain mode shapes was also lower.

Even though the results of these tests could not be used for the reasons that they were initially planned for, they serve as valuable lessons for the planning of new experiments.

4 Additional experiments for monitoring the crack formation

As mentioned in §1.4 an additional set of validation experiments was performed in order to evaluate the potential of BOFDA optical fibres in the framework of crack formation detection. In Figure 35 the results of the overall V9 BOFDA optical fibre are presented. The graph depicts the measurements obtained at the different deflections and at the different heights in the beam (lower measurement line indicated by "1" and the one at mid height by "2"). Also included in this graph are the measurements at the front (indicated by "s", which is on the DIC side) and those at the rear (indicated by "c").

In what follows, we will only zoom in on the results obtained at the front side as during the test, a certain load asymmetry was observed between the front and back side of the specimen, which had a significant/not negligible impact on the crack width developed on both sides of the beam and as the DIC set-up only allows alignment with the crack width on the front side, the focus of this report will only be on these results. In Figure 35 it can already be seen that from a certain strain value, large jumps in the measurements are present.

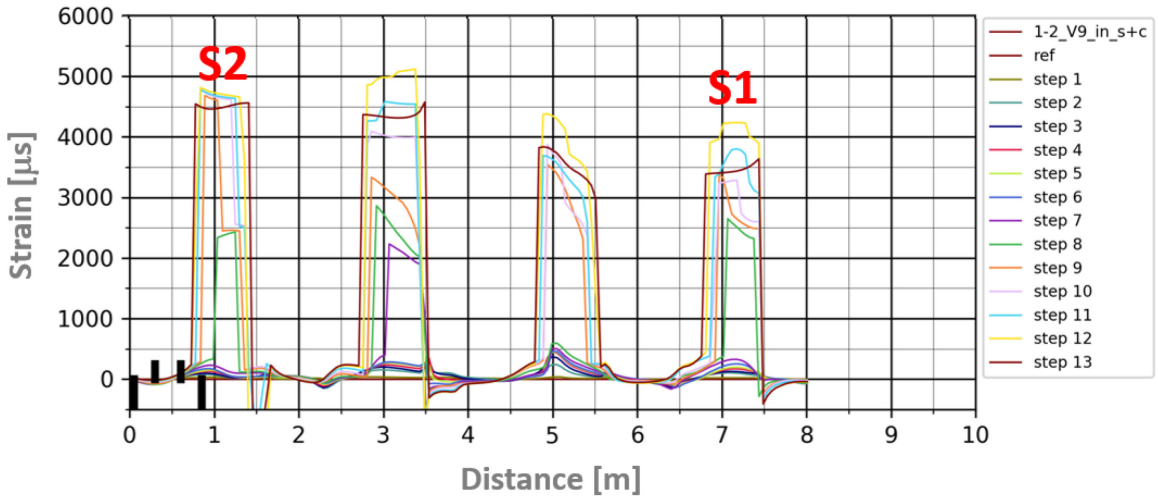

Figure 35. Overall results of the V9 BOFDA optical fibre during the course of the 4 point bending test (at different constant deflections).

Several analyses were performed with the measurement data. These included evaluation of the area under the measurement curve and the peak strain. The evaluation of the peak strain yielded the best correlations. These results are therefore discussed in more detail below. In Figure 36 the results of the BOFDA V9 measurement lines “s” are presented. To the right of this figure, a zoom can be found of the evolution of the measured strains “1-V9-in-s” at the different deflection steps along the length of the beam. Up to deflection step 7, a smooth evolution along the length of the beam can be observed. From step 8 onwards, sudden jumps are present in the measurement. In Figure 36 (left), the correlation between the BOFDA peak strain and the crack width measured at the concrete surface with the DIC is shown. In this graph, one can clearly observe that until deflection step 7 a linear correlation exists. From step 8 onwards, the correlation is completely lost.

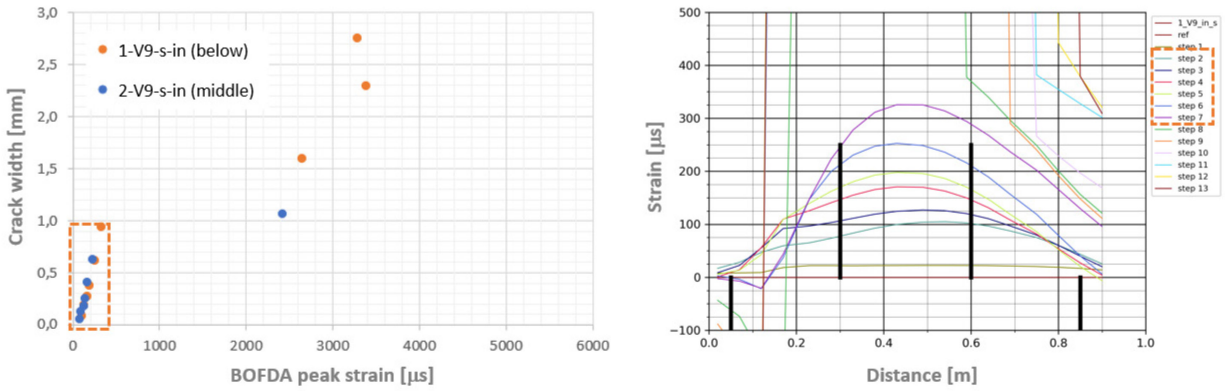

Figure 36. Detail of results of the BOFDA V9 measurement lines "s".

Up to a crack width of ± 1 mm, a fairly good linear regression (R^2 of 0.97) was observed between the peak strain of the BOFDA V9 and the crack width registered with the DIC, cf. Figure 37. When the data of the 2 measuring lines (the one at the bottom of the beam (s1) and the one at mid height (s2)) are combined (see Figure 37), a regression coefficient of 0.0036 is obtained. The intercept with the x-axis is situated around ± 80 µs, which also corresponds with the expected maximal tensile strain of the concrete (for C30/37 ≈ 80 µs (= f_{ctm}/E_{cm} = 2.9 MPa/33 GPa)). The latter additionally confirms the good correlation between the strain peak of the BOFDA V9 and the crack width of the DIC.

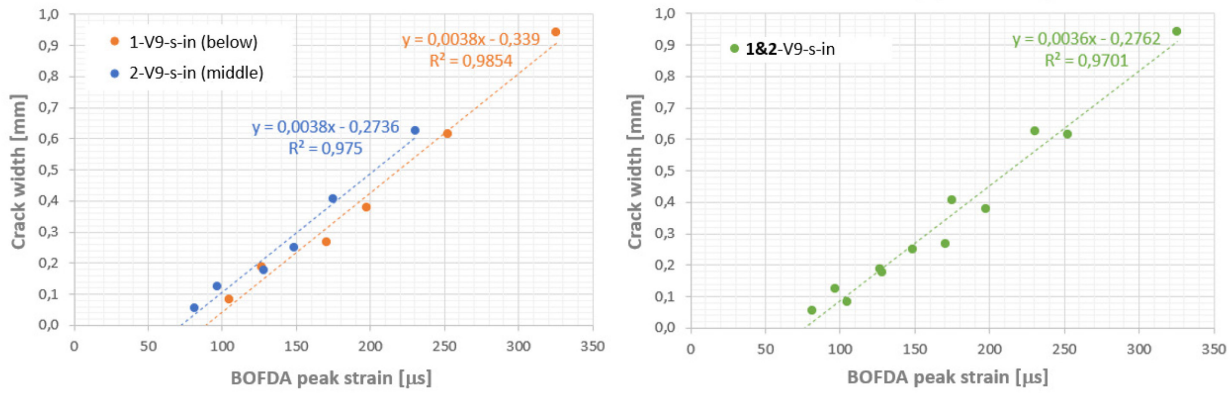

Figure 37. Linear regression of the of results of the BOFDA V9 measurement lines "s".

The same analysis was also carried out for the BOFDA Flat data. The results of this analysis can be found in Figure 38 and Figure 39.

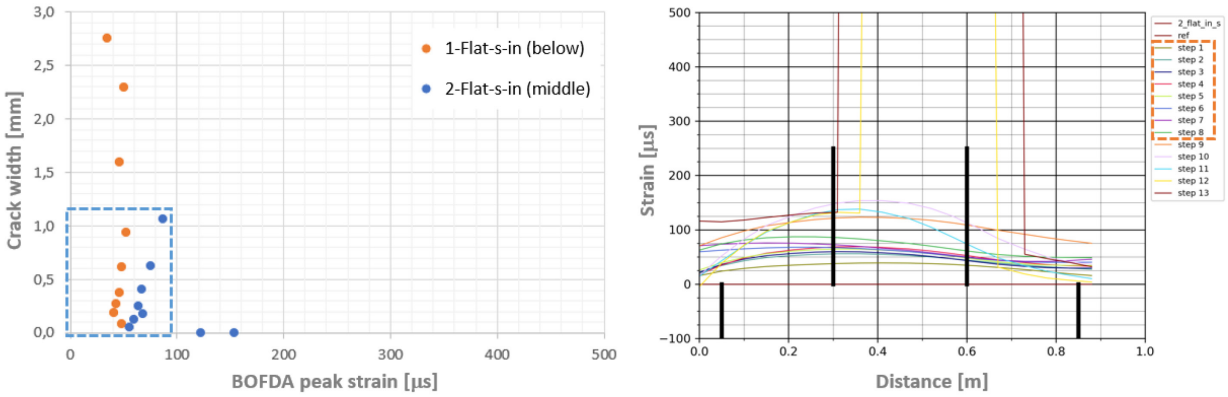

Figure 38. Detail of results of the BOFDA Flat measurement lines "s".

As was also observed for the BOFDA V9, the measurements show a important jump from a certain deflection. For the BOFDA Flat, this starts between step 8 and 9. A much weaker correlation was observed between the strain peak of the BOFDA Flat and the crack width. The linear regression delivers a much steeper slope than the one observed for the BOFDA V9. It can thus be stated that the BOFDA V9 is suitable for crack detection and approximate crack width determination. However in practice the occurring cracks need to be sufficiently spaced. An inter distance of more than 0.5 m is more or less needed. When mounted internally the BOFDA Flat is in no case suitable for crack detection.

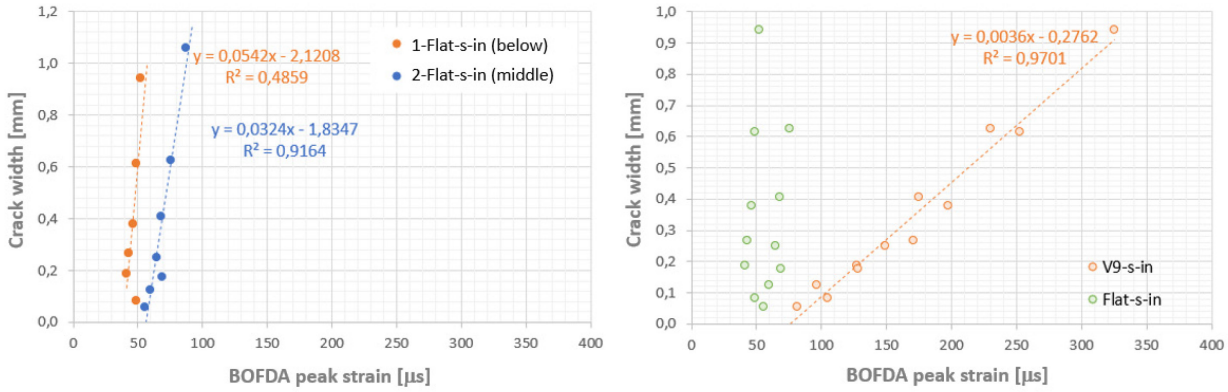

Figure 39. (left) Linear regression of the of results of the BOFDA Flat measurement lines "s" and (right) comparison with the BOFDA V9 linear regression.

A practical case in which this knowledge can prove highly useful is that of cracking in concrete basement walls due to restraint deformations. More details about this practical case can be found in §5.1.2 of the state-of-the-art. One of the basement walls monitored in the framework of the REINFORCE research project exhibited several restraint deformation cracks (see Figure 40). Typically these cracks are visually measured, which is a punctual and a highly approximated measurement. Based on the validation tests

presented above an estimate of the crack width was also performed by means of the BOFDA V9 monitoring data and compared with the visual crack measurements executed on the concrete surface.

Figure 40. Visual crack width determination on a basement wall as part of a monitoring campaign within the REINFORCE research project.

To allow for such a conversion the linear regression obtained true the validation experiments was converted to account for long term effects, specifically relaxation of the concrete. To this extend the tensile strength of the concrete was increased taking into account an estimated relaxation coefficient of 1,1 obtained on a similar concrete by means of a ring experiment (see Figure 41). The intercept with the X-axis of 80 µs as a result was increased to 170 µs. The regression coefficient is taken equal to the one found in the validation experiments as this parameters is only function of the crack width.

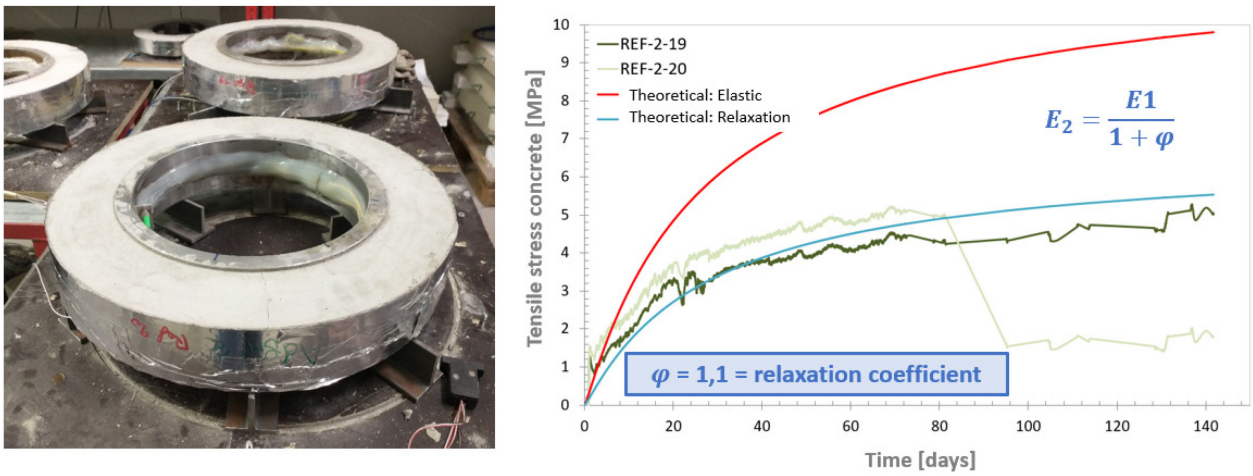

Figure 41. Estimation of the relaxation of the concrete by means of a ring experiment.

By means of this approach, based on the BOFDA V9 monitoring data a good approximation could be obtained of the in-situ realtime crackwidth, as can be seen in Figure 42.

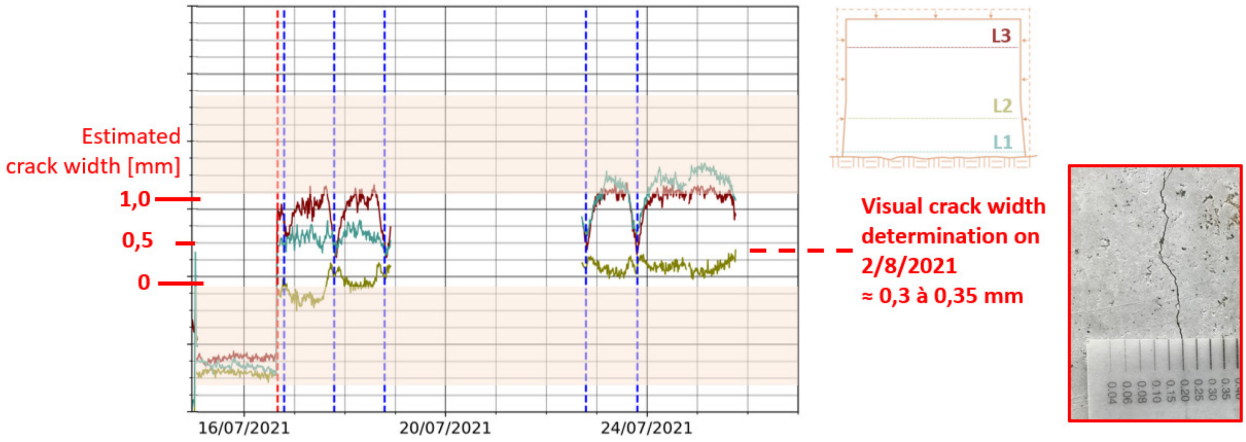

Figure 42. Estimation of the crack width of crack 2 by means of the BOFDA V9 monitoring data, based on the validation experiments executed on notched beams.

This monitoring data also demonstrates the relative nature of a punctual visual measurement. The monitoring data clearly shows that the actual crack width highly fluctuates throughout the day, in function of a complex mix of boundary and environmental conditions.

Annex 1. Simulated beams

The three simulated beams (B01 – B03) were all undergoing active corrosion, but differed in the damage and loading. Beam B01 was undamaged before the start of the corrosion, while beam B02 and B03 were precracked in a four-point bending (4PB) setup to an crack width of 0.2 mm. Upon unloading, a crack width of 0.04 mm remained at multiple cracks in the zone of constant bending moment. Furthermore, beam B03 is subjected to a sustained creep loading in a 4PB setup during the corrosion. The dimensions of all beams are the same with a height of 400 mm, a width of 300 mm and a span of 3000 mm. The distance between the loading points in the 4PB test is 1500 mm. The tensile and compressive reinforcement consists of 3x20 mm and 2x10 mm threaded rebars, respectively. Stirrups are present every 200 mm, with a diameter of 10 mm.

Finite element model parameters

Assumptions and model construction

In order to reduce the computational time, a 2D plane-stress analysis is set up. In such an analysis, the stresses along the width (i.e. *z*-coordinate) of the beam is assumed to be zero. It should be noted that this assumption cannot account for the splitting stresses that form around the rebars during the active corrosion process, and as such simplify the stress buildup around the rebars.

Material properties

The concrete is modelled in a non-linear material model based on the Model Code 2010 constitutive laws in compression and tension for a given strength class. This material model allows tensile cracking based on a rotating total strain based model along the principal stress axes, and compressive crushing. Creep and shrinkage behavior is based on the notional member size and the relative humidity of the environment (RH = 60 %). The bulk material is based on a strength class of C30/37, while the effect of corrosion damage in the zone around the tensile rebar is accounted for by lowering the strength class of the surrounding concrete to C12/15.

The predamage in beams B02 and B03 is taken into account by explicitly modelling triangular voids (i.e. cracks) in the mid-span, with a nominal width of 0.04 mm at the bottom of the beam.

The steel rebars are modelled with a perfect linear-plastic material behavior with Von Mises yielding at a yield strength of 500 MPa. The Young's modulus is equal to 210 GPa. Corrosion is taken into account by decreasing the steel surface area as a function of time, and based on the predicted mass loss from the experimental testing.

Loading, supports and convergence criteria

The beam is simply supported and in the case of B03, a load of 12 kN is applied at the two loading points. The corrosion process is divided in 150 logarithmically spaced time steps (up to 600 days) and convergence is attained in each time step by simultaneously satisfying a force and displacement criterion of 0.01 in a Quasi-Newton (BFGS) method.

Results

The results are compared for the measured vs predicted tensile strain at the rebars in the mid-span of the beam. The results are shown in the figure below.

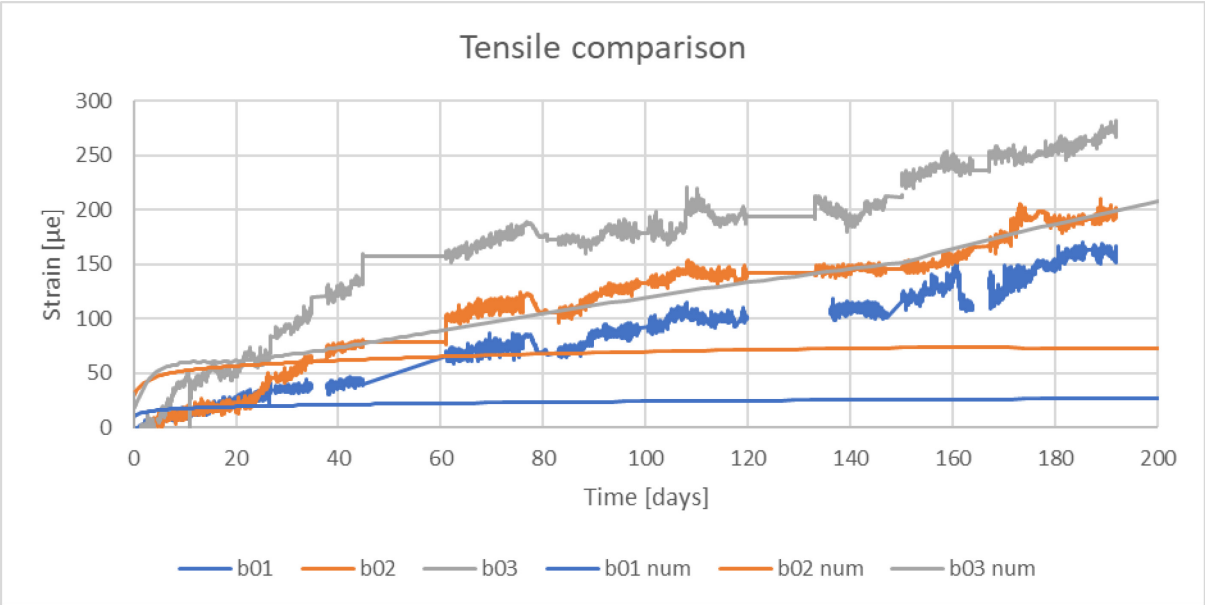

It is clear that increasing the damage (B01 -> B02) leads to higher measured strains, and applying an additional loading to the specimen (B02 -> B03) further increases the tensile strains. However, the evolution of the strain increase in time is not well captured for the non-creeping beams, where the model underpredicts the strain increase. This might be due to localized effects (pitting corrosion or water absorption) which require more detailed characterization and modelling approaches. Nevertheless, the result show that the creep behavior still dominates for beam B03 as can be seen from the increasing strain measurement values. Note also the change in strain increase around 150 days which corresponds to a higher imposed current driving the corrosion process.

In conclusion, numerical modelling can be a useful tool to better understand and assess the structural behavior of corroding reinforced concrete beams, and with proper understanding and calibration, can predict similar strain values as measured in experimental testing.